Volume 16
Number 23
21 June 2024
Pages 10867-11354

Nanoscale

rsc.li/nanoscale

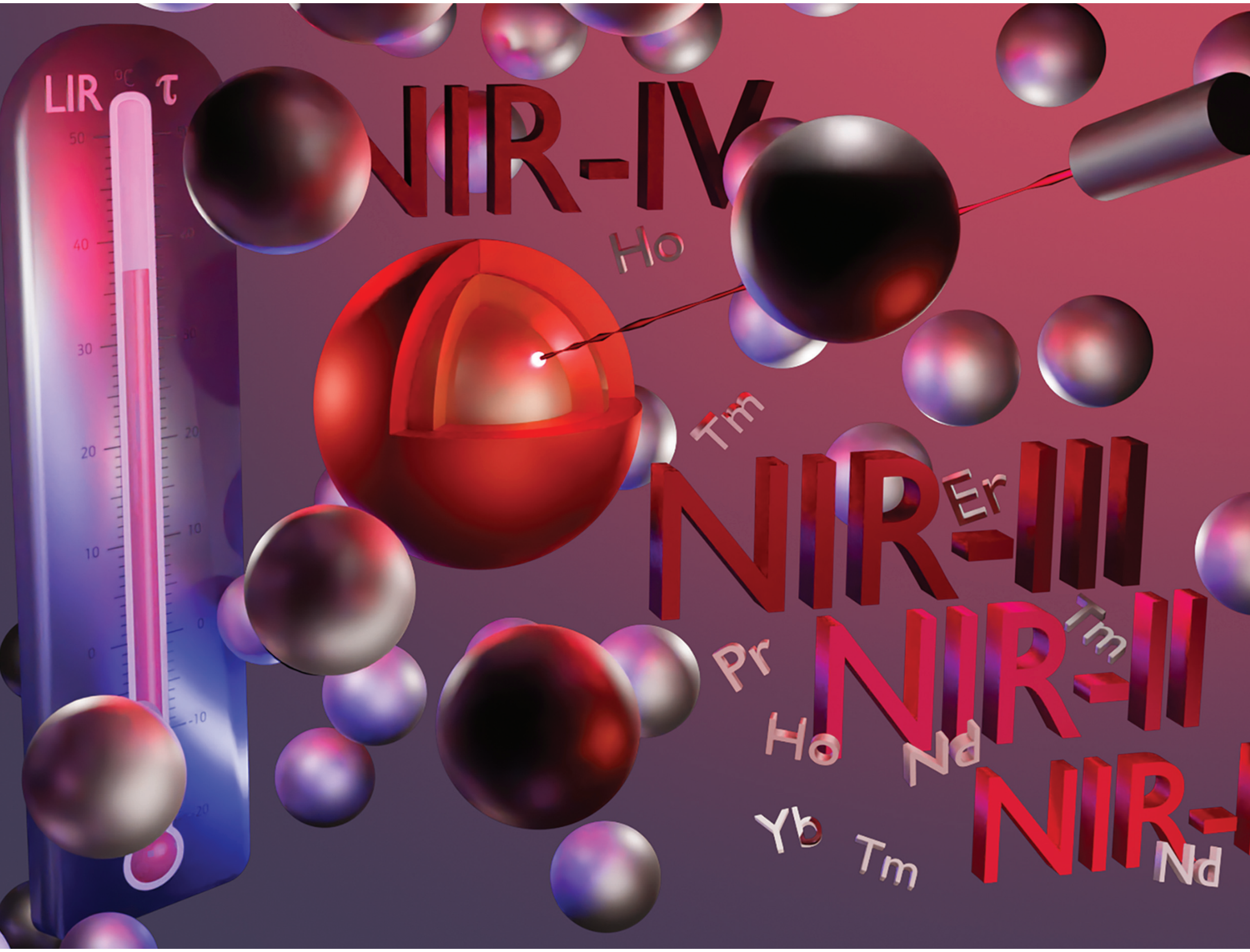

ISSN 2040-3372

ROYAL SOCIETY
OF **CHEMISTRY**

MINIREVIEW
Eva Hemmer *et al.*
Lanthanide-based nanomaterials for temperature sensing in the near-infrared spectral region: illuminating progress and challenges

NCNST

Nanoscale

MINIREVIEW

View Article Online
View Journal | View Issue

Cite this: *Nanoscale*, 2024, **16**, 10975

Lanthanide-based nanomaterials for temperature sensing in the near-infrared spectral region: illuminating progress and challenges

Abigale Puccini, Nan Liu and Eva Hemmer*

Being first proposed as a method to overcome limitations associated with conventional contact thermometers, luminescence thermometry has been extensively studied over the past two decades as a sensitive and fast approach to remote and minimally invasive thermal sensing. Herein, lanthanide (Ln)-doped nanoparticles (Ln-NPs) have been identified as particularly promising candidates, given their outstanding optical properties. Known primarily for their upconversion emission, Ln-NPs have also been recognized for their ability to be excited with and emit in the near-infrared (NIR) regions matching the NIR transparency windows. This sparked the emergence of the development of NIR-NIR Ln-NPs for a wide range of temperature-sensing applications. The shift to longer excitation and emission wavelengths resulted in increased efforts being put into developing nanothermometers for biomedical applications, however most research is still preclinical. This mini-review outlines and addresses the challenges that limit the reliability and implementation of luminescent nanothermometers to real-life applications. Through a critical look into the recent developments from the past 4 years, we highlight attempts to overcome some of the limitations associated with excitation wavelength, thermal sensitivity, calibration, as well as light-matter interactions. Strategies range from use of longer excitation wavelengths, brighter emitters through strategic core/multi-shell architectures, exploitation of host phonons, and a shift from double- to single-band ratiometric as well as lifetime-based approaches to innovative methods based on computation and machine learning. To conclude, we offer a perspective on remaining gaps and where efforts should be focused towards more robust nanothermometers allowing a shift to real-life, *e.g.*, *in vivo*, applications.

Received 20th January 2024,
Accepted 4th April 2024

DOI: 10.1039/d4nr00307a

rsc.li/nanoscale

Introduction

Detection of temperature with high thermal and spatial resolution is necessary for a wide range of industrial and research applications, including microelectronics, nanofluidics, and biomedicine.[1–4] Conventional contact thermometers, which are considered an invasive thermal sensing technique, are not suitable when temperature is measured at scales below 10 μm.[5] To overcome this limitation, remote, minimally invasive luminescence nanothermometers have been developed to allow for local temperature sensing at the nanoscale.[6] Luminescence nanothermometry refers to a spectroscopic technique in which temperature-dependent changes in the spectral features of an optical nanoprobe, *e.g.*, emission intensity, lifetime, spectral shape, or peak position, can be used to provide a remote thermal readout.[6–8] Using luminescence nanothermometry, temperature can be sensed in applications where conventional contact thermometers are ineffective, such as in harsh environmental conditions, in fast moving objects, and in the presence of strong electromagnetic fields.[9] It has also proven to be promising for remote *in vitro* or even *in vivo* thermal sensing.[4] The possibility for remote and minimally invasive temperature sensing has resulted in growing exploration of different materials and molecules capable of acting as luminescence thermometers at the nanoscale in recent years. Seminal work on the field of luminescence thermometry began in the early 1930s,[10] however breakthroughs in the field appeared in the early 2000s, with a significant boom in publications between 2007 and 2012.[2,6,7] The first review papers were generated during this time, with seminal work by Brites *et al.* outlining guidelines for luminescence nanothermometry towards standardizing the field.[7]

To date, organic dyes, quantum dots, polymers, and lanthanide(Ln)-based molecules, molecular cluster-aggregates, and nanoparticles (NPs) have been examined as candidates for luminescence nanothermometry.[6,11–16] Among these, Ln^{3+}-

---

Department of Chemistry and Biomolecular Sciences, University of Ottawa, Ottawa, ON, Canada. E-mail: ehemmer@uottawa.ca

based molecules and NPs are the most explored candidates for luminescence nanothermometry. In lanthanide-based NPs (Ln-NPs), the optically active Ln^{3+} ions are doped into an inorganic crystalline host lattice, such as oxides, chlorides, bromides, vanadates, oxysulphides, oxychlorides, and fluorides, with the latter being most popular owing to its low phonon energy, accessible synthesis routes, and good thermal and chemical stability.[17,18] Characterized by an incomplete 4f shell shielded by the outer $5s^2$ and $5p^6$ shells, the influence of the host lattice and surrounding environment on the optical properties of Ln^{3+} ions is minimized. This results in long excited state lifetimes and narrow absorption and emission bands that favour the use of excitation wavelengths in the near-infrared (NIR) and leads to emission of light in the ultraviolet (UV), visible, and NIR spectral regions.[19] Nonetheless, temperature has been found to influence the spectral features of the Ln^{3+} ions due to phonon-assisted changes in the population of the emitting energy levels, energy transfer, non-radiative relaxation, or cross-relaxation, ultimately allowing for an optical readout of temperature.[29] By tailoring the choice of Ln^{3+} dopants, NIR-to-visible upconversion (UC) and NIR-to-NIR wavelength conversion become possible, allowing for excitation and emission in the so-called optical transparency windows (also referred to as biological windows, BWs). While there is no clear consensus about the definition of these NIR transparency windows, the spectral region from 700–950 nm is commonly defined as NIR-I, that from 1000–1350 nm as NIR-II, and NIR-III spans the 1550–1870 nm spectral range (Fig. 1A and B). The recently added 4th window, NIR-IV, covers the 2050–2400 nm spectral region.[30–32] The tunability of both excitation and emission wavelength from shorter to longer renders Ln^{3+}-doped materials excellent candidates for thermal sensing at the nanoscale – though, challenges remain. For example, the overlap of Ln^{3+} emission bands residing in the

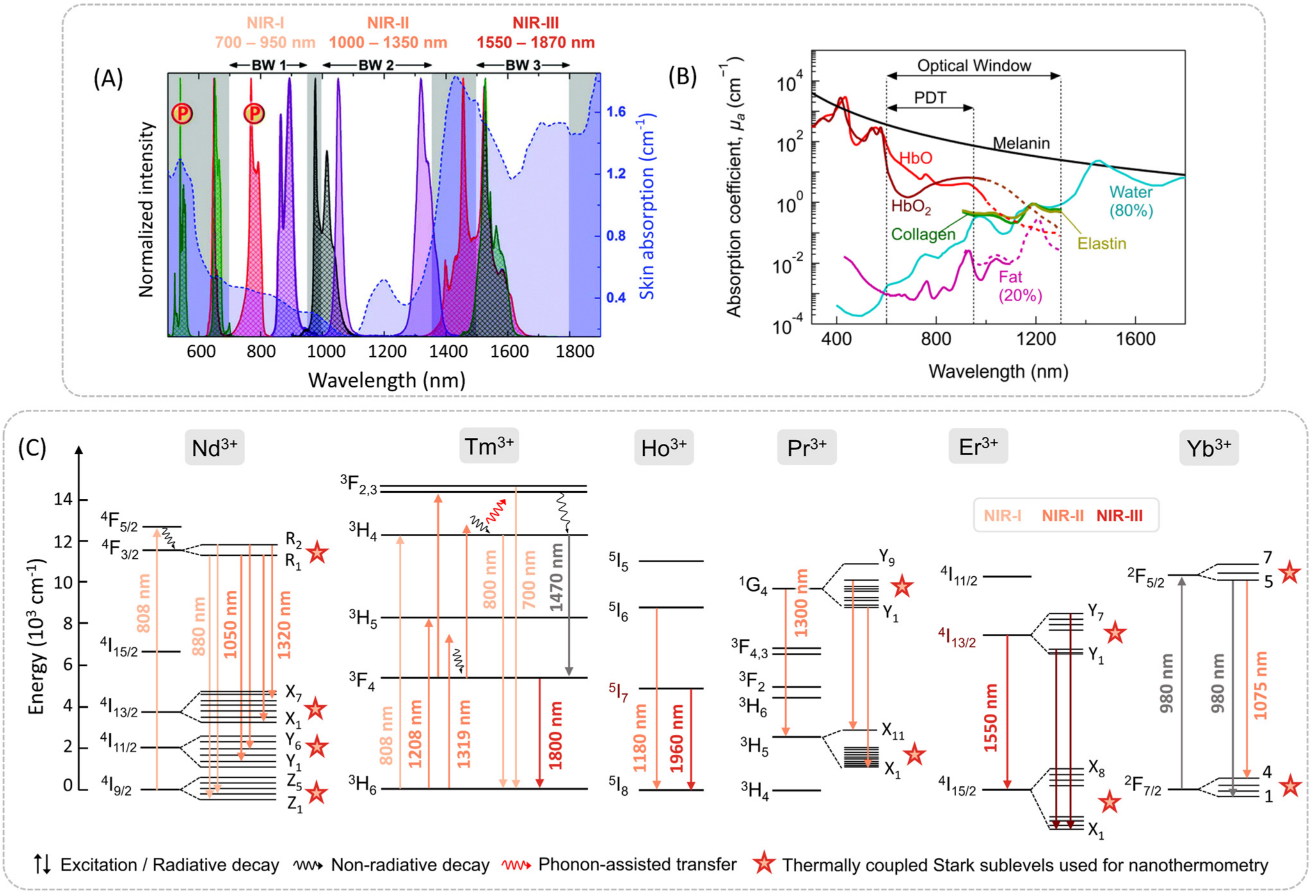

Fig. 1 (A) Optical transparency windows (biological windows, BWs) and normalized emissions of Yb^{3+} (black), Nd^{3+} (purple), Yb^{3+}/Er^{3+} (green) and Yb^{3+}/Tm^{3+} (red) doped in SrF_2 host material. Wavelength-specific artefacts that can affect the reliability of thermal sensing are also indicated, *i.e.*, emissions with excitation power dependent spectral shape (indicated by the red 'P' circle) and emission bands susceptible to undergoing self-absorption (grilled filling of the curve). Grey backgrounds denote the spectral ranges out of the BWs of transparency. The absorption of skin (in cm^{-1}) is shown by the dashed blue line. Reproduced from ref. 20 with permission from Royal Society of Chemistry, copyright 2022. The NIR spectral regions corresponding to the definition of the biological windows used in this review are added to the top of the figure. (B) The absorption of main biological molecules spanning from the visible to NIR spectral region. Reproduced from ref. 21 with permission from MDPI, copyright 2021. (C) Schematic representation of the energy levels and f-f transitions in NIR-NIR thermometers based on Nd^{3+}, Tm^{3+}, Ho^{3+}, Pr^{3+}, Er^{3+}, and Yb^{3+}. Redrawn based on ref. 22–28.

BWs with the absorption of human skin (Fig. 1A) shows the susceptibility of these emission bands to be altered by the medium and environment, including water, as well as biological components present (Fig. 1B).[20] This can result in distortion or modification of the spectra, which can limit the reliability of a nanothermometer, ultimately leading to false temperature readouts. Therefore, care must be taken to select Ln^{3+}-dopants for nanothermometry applications that avoid or minimize the influence of environmental or experimental effects on the emission spectra. Nonetheless, some reports demonstrated excellent imaging capabilities in the NIR spectral regions that overlap with tissue and water absorption bands. In particular, the Ln^{3+} emissions residing in the gaps between the BWs, *i.e.*, the emissions of Yb^{3+}, Ho^{3+}, Tm^{3+}, and Er^{3+} that overlap with the water absorption bands present around 980, 1200, 1450, and 1930 nm (Fig. 1B), showed excellent bioimaging quality due to absorption-induced resolution and contrast enhancements,[33–35] which would also benefit spatial resolution when aiming for thermal mapping.

Many research efforts focus on harnessing the NIR-to-visible UC ability of Ln^{3+} ions for nanothermometry approaches, with reviews summarizing achievements made.[2,6,7,36–38] However, with growing interest in using Ln-NPs as nanothermometers for biomedical applications, there has been a need for luminescence nanothermometers that undergo NIR-to-NIR wavelength conversion, which is the subject of this mini-review. Herein, we summarize the recent developments of Ln^{3+}-based NIR-NIR nanothermometers, focusing on achievements made over the past 4 years. First, the most important thermometric parameters will be briefly introduced. We will then showcase recent advances in nanothermometry based on the widely explored ratiometric luminescence approach, followed by lifetime-based and other, unconventional strategies that recently emerged, highlighting how challenges and limitations encountered in the past have been addressed towards more sensitive and more reliable thermal sensors, while also critically assessing remaining challenges.

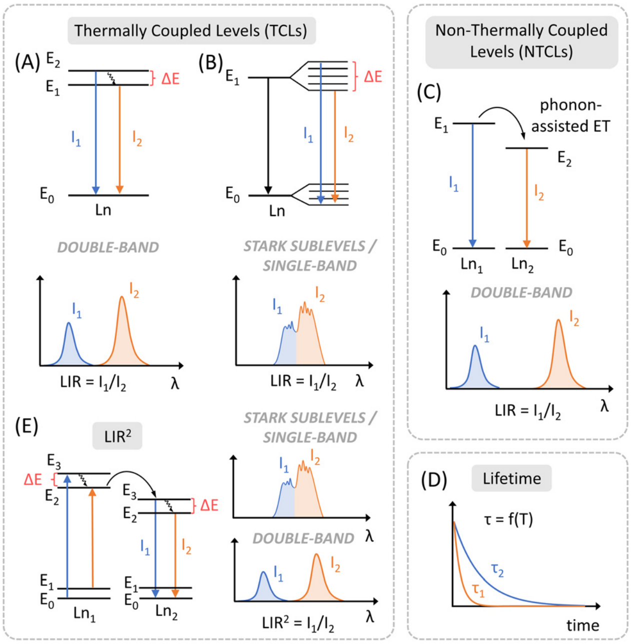

Fig. 2 Schematic overview of luminescence nanothermometry approaches discussed in this review. (A) Double-band and (B) single-band nanothermometry based on thermally coupled levels (TCLs). (C) Double-band nanothermometry based on non-thermally coupled levels (NTCLs). (D) Lifetime-based nanothermometry. (E) A recently proposed LIR^2 approach based on TCLs.[27]

Fundamental aspects of nanothermometry

Figures of merit

While excellent review papers and book chapters have been published to which the interested reader is referred to for an in-depth discussion, the basic parameters used to describe the thermometric performance are briefly introduced in the following.[2,5,37–39]

Relative thermal sensitivity, S_r. Ratiometric approaches are widely applied as they are less affected by emitter concentration when compared to thermal sensing based on absolute emission intensity.[40] Herein, the thermometric parameter is the luminescence intensity ratio, LIR, commonly used to quantify a nanothermometer's thermometric performance. The LIR can be quantified as the ratio between the integrated intensities of two emission bands that originate from two different and distant energy levels (double-band approach, also referred to as dual-band) or two Stark sublevels (single-band approach) (Fig. 2A–C). A key figure of merit is the relative thermal sensitivity (S_r), which correlates the change in LIR with change in temperature. This quantitative parameter is used to assess and compare the performance of different thermometers. It is defined as:

$$S_r = \frac{1}{\mathrm{LIR}}\frac{\partial \mathrm{LIR}}{\partial T} \tag{1}$$

For Ln-NP-based NIR double-band nanothermometers, S_r values greater than 1% K^{-1} are currently considered as indicative of a sensitive nanothermometer.[2] While the S_r values of single-band nanothermometers are intrinsically lower than those of double-band nanothermometers (typically <1% K^{-1}), being restricted by the value of ΔE (Fig. 2B). Following a lifetime-based approach (Fig. 2D), τ, the luminescence lifetime, can replace LIR in eqn (1) to calculate S_r.

Thermal resolution or temperature uncertainty, δT. Besides S_r, thermal resolution (also referred to as temperature uncertainty), δT, representing the smallest temperature change that can be resolved in a given measurement, is another important figure of merit. Depending on the experimental detection setup used, the acquisition conditions applied, and the signal-to-noise ratio in the experiment, δT might change. While there is still no full consensus within the nanothermometry community on how to standardize the determination of δT, it is often calculated by:

$$\delta T = \frac{1}{S_r}\frac{\delta \text{LIR}}{\text{LIR}} \tag{2}$$

Herein, δLIR/LIR is the relative uncertainty over the thermometric parameter. For LIR-based thermometry, δLIR/LIR is obtained as:

$$\frac{\delta \text{LIR}}{\text{LIR}} = \sqrt{\left(\frac{\delta I_1}{I_1}\right)^2 + \left(\frac{\delta I_2}{I_2}\right)^2} \tag{3}$$

In general, the value of δT of a nanothermometer should be smaller than 1 K to achieve the sensitivity requirement.[5] However, methods to obtain δT are diverse and thus must be considered with care when using them to compare different nanothermometer systems.[41]

Repeatability, *R*. The repeatability, R, describes the thermometer's ability to provide repeatedly the same result, under the same circumstances. This value generally should be higher than 90% for good repeatability.

$$R = 1 - \frac{\max(|\text{LIR}_i - \text{LIR}_{\text{mean}}|)}{\text{LIR}_{\text{mean}}} \tag{4}$$

where LIR_i is the luminescence intensity ratio at a given temperature measured for the i-th round of measurement, and LIR_{mean} is the average obtained from i independent measurements.

The aforementioned thermometric parameters can be affected by numerous environmental and experimental factors.[20] For instance, solvent (non-aqueous solvents, water, or dry powder) has a significant impact on the performance of nanothermometers,[11,20] hence, it is important to be aware of the environment in which the thermal performance of a thermometer is reported.

Ratiometric approaches: thermally coupled *versus* non-coupled levels

When the energy gap (ΔE) between the two electronic transitions is between 200 and 2000 cm^{-1}, they are considered thermally coupled levels (TCLs), and their dependence on temperature can be used to quantify a thermal readout based on a ratiometric Boltzmann governed approach (Fig. 2A and B). Probably the most popular example are the two green-emitting energy levels of Er^{3+} ($^4S_{3/2}$ and $^2H_{11/2}$). Though originating from two distinct f–f transitions, they are in close proximity to be thermally coupled and the resultant LIR follows Boltzmann distribution.[6] When the thermally coupled emissions arise from the Stark sublevels of a single Ln^{3+} emission band, its temperature can be quantified following a single-band ratiometric approach. For instance, this is the case for some Nd^{3+} nanothermometers that use thermalized energy states originating from the same emission band between Stark sublevels (Fig. 1C).[22] When following a Boltzmann governed approach, the thermal sensitivity of a nanothermometer system is directly proportional to the ΔE between the TCLs, implying that higher S_r values can be achieved when using TCLs with larger energy gaps (eqn (5)).[39]

$$S_r = \frac{\Delta E}{k_B T^2} \tag{5}$$

where ΔE is the energy gap separating the thermally coupled electronic levels, k_B is Boltzmann's constant (0.69503476 cm^{-1} K^{-1}), and T is temperature in Kelvin. Consequently, TCLs with ΔE less than 200 cm^{-1} suffer from low S_r values, as is the case for the two Nd^{3+} NIR Stark emissions stemming from the $^4F_{3/2}$ manifold, but also for single-band nanothermometers based on Tm^{3+} or Er^{3+}.[24–26] Therefore, over the past decade, several strategies have been employed to increase S_r of nanothermometers based on TCLs by optimizing ΔE. Notably, recent work by Suta *et al.* addressed the common pitfalls of single emitting Nd^{3+}-based nanothermometers for *in vivo* applications.[42] They observed that the thermally coupled Stark sublevels of the Nd^{3+} $^4F_{3/2}$ manifold have a very small ΔE and consequently resulted in S_r values too low for *in vivo* thermal sensing. They noted that when previous works used co-doped sensitizing Yb^{3+} or Er^{3+}, alongside Nd^{3+}, as a strategy to improve S_r by facilitating phonon-assisted energy transfer, the Boltzmann relationship of the TCLs was lost and overlap between temperature-dependent emissions was observed, ultimately resulting in inaccurate thermal resolution. Therefore, the authors proposed a Boltzmann governed nanothermometer that uses the thermal coupling between the $^4F_{3/2}$ and $^4F_{5/2}$ Nd^{3+} levels. A larger ΔE was realized for these TCLs (~1000 cm^{-1}) and in turn produced S_r values above 1% K^{-1} in the physiological regime (Fig. 3A, top). The authors took care to select a host lattice (LaPO$_4$) with phonon energy similar to the ΔE of the TCLs (~1050 cm^{-1}) to allow for resonant thermalization of the TCLs. The authors also concluded that a low Nd^{3+} dopant concentration (< 0.02 mol%) was necessary to maintain a Boltzmann equilibrium between the TCLs over the physiological temperature range, since the investigated TCLs demonstrated efficient cross-relaxation quenching at higher dopant concentrations that competes with the non-radiative decay that governs thermalizations (Fig. 3A bottom).

From double-band to single-band nanothermometry. Regardless of thermal sensitivity limitations resulting from smaller ΔE, nanothermometers based on the single-band emission of Ln^{3+} ions (*i.e.*, Stark sublevels) offer advantages over double-band nanothermometers when considering application in the life sciences. When the thermometric performance is quantified based on temperature-dependent changes stemming from the TCLs of a single NIR emission, there is equal heterogenous attenuation of the levels from biological media and tissue.[26,44] This allows for the calibration to be maintained, despite optical inhomogeneity of the tissues. This contrasts with a double-band ratiometric approach, where the temperature-dependent emissions often reside in different NIR regions, and thus the two NIR emissions used to quantify a thermal readout are attenuated differently, resulting in an inaccurate and falsely calibrated temperature readout. Therefore, when considering thermal sensing for biological

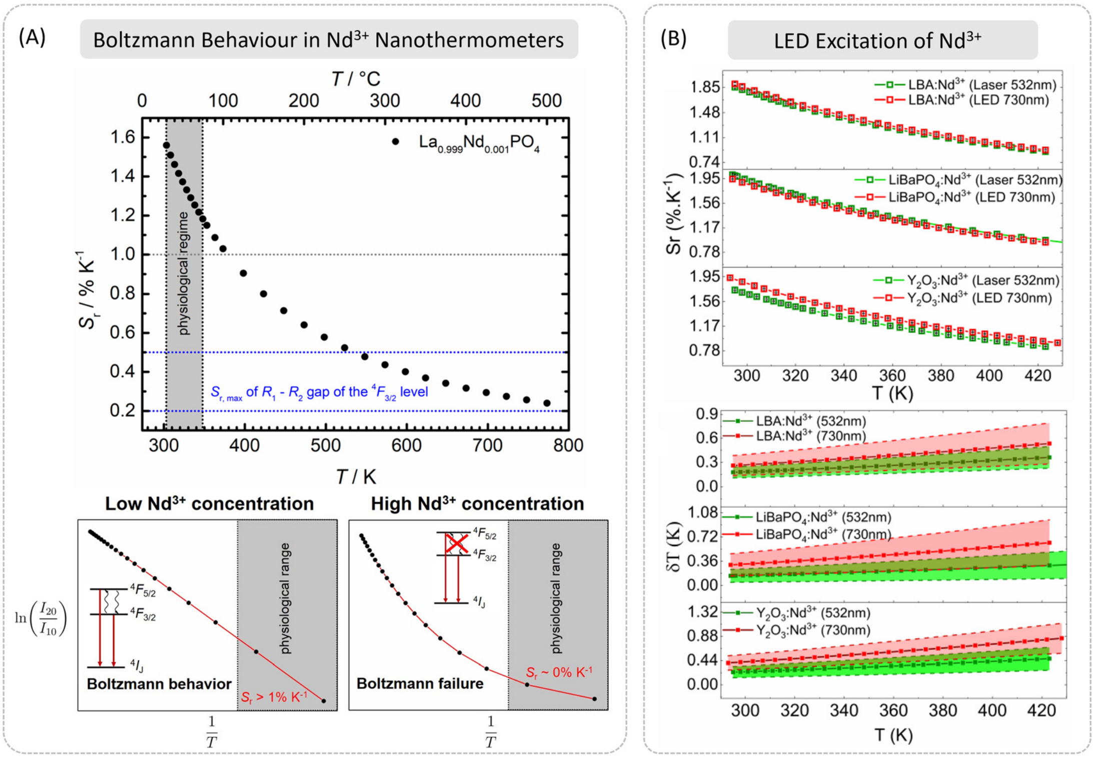

Fig. 3 Improving the thermometric performance of Nd^{3+}-based NIR-I thermometers focusing on TCLs and alternate excitation sources – (A) (top) relative thermal sensitivity (S_r) for the Boltzmann governed nanothermometer based on the TCLs of the Nd^{3+} $^4F_{3/2}$ and $^4F_{5/2}$ manifolds (solid black dots) compared to the maximum S_r based on the thermally coupled Stark sublevels of the Nd^{3+} $^4F_{3/2}$ manifold (dashed blue line), which shows insufficient S_r values in the physiological range for *in vivo* nanothermometry. (bottom) Boltzmann equilibrium is maintained when using low Nd^{3+} dopant concentrations. Host material: $LaPO_4$. Reproduced from ref. 42 with permission from MDPI, copyright 2023. (B) (top) Relative thermal sensitivity (S_r) obtained when using 730 nm LED (red lines) *versus* 532 nm laser excitation (green lines) of Nd^{3+} doped into three different host materials, *i.e.*, lithium-boron aluminium (LBA) glass, $LiBaPO_4$, and Y_2O_3. (bottom) Irrespective of the chosen host material, superior thermal resolution (δT) was obtained when using 730 nm LED (red lines) *versus* 532 nm laser excitation (green lines). Reproduced from ref. 43 with permission from MDPI, copyright 2020.

applications, research has shifted to developing single-band nanothermometers, particularly to those that operate at wavelengths longer than 1000 nm. Some notable examples are highlighted further below.

Ln^{3+} ion choice based on excitation wavelength

From Yb^{3+} to Nd^{3+}-excited nanothermometers

Activator ions such as Nd^{3+}, Tm^{3+}, Ho^{3+}, and Er^{3+} are known for their NIR emission bands that are suitable for NIR-NIR nanothermometry (Fig. 1C), whereas Yb^{3+}, which is excitable at 980 nm, is often chosen as a co-doped sensitizer ion due to its relatively large absorption cross-section.[2] The Yb^{3+} ion also has a NIR emission at *ca.* 980 nm and is often explored as a co-dopant with other Ln^{3+} activators to undergo a double-band ratiometric approach.[45,46] Moreover, the single Yb^{3+} emission has been used for nanothermometry following bandshift and lifetime-based approaches, the latter being described more in depth later.[46–50] Despite the popularity of Yb^{3+} as sensitizer ion, a major drawback is the relatively strong absorbance of 980 nm light by water and biological species, resulting in the risk of localized heating effects and limited penetration depth, ultimately rendering Yb^{3+} sensitized emitters less favourable when targeting biological applications.[51] Therefore, the 980 nm emission of Yb^{3+} is often excluded from definitions of the BWs, as this wavelength falls between two windows, with the NIR-I region ending at 950 nm and the NIR-II region beginning at 1000 nm (Fig. 1A). To overcome this limitation, researchers sought to explore alternative Ln^{3+} sensitizing ions allowing for less damaging and deeper penetrating excitation wavelengths. For instance, seminal work demonstrated the sensitizing ability of Nd^{3+} under 808 nm excitation, which is less absorbed by water.[52–54] Since then, Nd^{3+} gained significant popularity and has been doped or co-doped into various nanomaterials, whereas its thermal sensing abilities have been extensively explored.[51,55,56] In addition to excitation at 808 nm, Nd^{3+} ions conveniently emit in the NIR-I region around 880 nm ($^4F_{3/2} \rightarrow {}^4I_{9/2}$) as well as in the NIR-II region around 1050 nm ($^4F_{3/2} \rightarrow {}^4I_{11/2}$) and 1320 nm ($^4F_{3/2} \rightarrow {}^4I_{13/2}$). What makes Nd^{3+} so versatile for nanothermometry is that the different emissions allow for different thermometric approaches to temperature sensing. Importantly, by using

808 nm excitation over 980 nm excitation sources, it has been demonstrated that minimizing overheating effects from water absorption led to improved thermometric performance of these nanothermometers.[51] Alternatively, Laia *et al.* proposed the use of 730 nm LED light as an excitation source to foster the Nd^{3+} NIR-I emission (Fig. 3B, top).[43] Nd^{3+} excitation using 750 nm laser sources was previously reported by other groups,[57,58] but the authors noted the limited availability of this laser on the market and its associated increased cost compared to a 730 nm LED. Even when using 730 nm LED excitation, higher maximum S_r values (1.94% K^{-1}) were achieved using the proposed Nd^{3+}-doped nanothermometer compared to other studies reporting the use of 750 nm laser excitation (1.32 and 1.7% K^{-1}).[57,58] Even though LED excitation provided limited stability of the emission intensities, the LIR method could still be applied as one luminescence band was used as a reference for the other. Through their proof-of-concept study, the authors successfully demonstrated how alternate excitation sources can be used to obtain high thermal sensitivities following a Nd^{3+}-based ratiometric approach. Notably, they achieved slightly better S_r values (Fig. 3B, top) and significantly better thermal resolution (δT) when using 730 nm LED light compared to using 532 nm laser excitation (Fig. 3B, bottom). Regardless, LED excitation often results in low power density compared to laser excitation sources and triggering bright and efficient Ln^{3+} ion excitation is therefore difficult to achieve. Nonetheless, with the development of more powerful LED sources and more efficient Ln-NPs, there is potential for a shift toward simpler, more cost-efficient setups that allow for easier implementation of nanothermometry to real-life applications.

Beyond Yb^{3+} and Nd^{3+}: Tm^{3+}-based nanothermometers excited with longer wavelengths

Tm^{3+} stands out given the multiple excitation wavelengths suitable to generate NIR emission bands, *i.e.*, 808, 1210, and 1319 nm (Fig. 1C).[23–25,59,60] The benefits of 808 nm as excitation source have been outlined above, however, compared to Nd^{3+}, the absorption cross section of Tm^{3+} at 808 nm is relatively low.[38] Consequently, Tm^{3+}-sensitized NIR emissions often suffer from low signal-to-noise ratios, which hampers thermometric performance.[38] Therefore, the use of excitation wavelengths longer than 980 nm, such as 1210 and 1319 nm, are of interest, particularly for – but not limited to – biomedical applications as they permit greater penetration depth into and less scattering by tissues and other environments.[30,31] A potential drawback of these longer wavelength is the increasing water absorption, with an absorption coefficient of water at 1208 nm approximately equal to that at 980 nm (Fig. 1B). Nonetheless, the reduced scattering and absorbance of light by biological components that comes with the use of longer wavelengths may outbalance this disadvantage. In fact, there are a few successful examples that demonstrate the thermal sensing capability of Tm^{3+}-doped NPs for NIR-NIR nanothermometry under aforementioned longer excitation.[24,25,59,60] Herein, under 1210 nm excitation, a higher maximum S_r was achieved compared to 1319 nm excitation (2.64% K^{-1} *versus* 0.80% K^{-1}).[24,25] While taking advantage of the longer excitation wavelengths, the upconverted NIR-I emission bands associated with the Tm^{3+} $^3F_{2,3} \rightarrow {}^3H_6$ and $^3H_4 \rightarrow {}^3H_6$ transitions (centred at 700 and 800 nm, respectively), were used to determine the thermometric parameters based on a LIR approach. The Stark sublevels of the $^3H_4 \rightarrow {}^3H_6$ manifold following the Boltzmann distribution law were also investigated. However, matching the NIR-I spectral region, a rather low signal-to-noise ratio and limited penetration through biological samples were reported for the emitted light. The researchers further explored the effect of excitation power density on the thermometric performance under 1319 nm Tm^{3+}-sensitized excitation. Due to the non-resonant match of the pump photon energy with the energy of the NIR-I emitting levels of Tm^{3+}, the 1319 nm excitation source was only weakly absorbed by the Tm^{3+} ions. In the investigated laser power density regime (~14–40 kW cm^{-2}), no emission intensity saturation effects were observed, allowing for the use of higher laser power to achieve good signal-to-noise ratios and in turn enhanced thermal sensing performance. This contrasts 980 nm excitation, in particular when considering the Yb^{3+}-sensitized emission of Er^{3+}, where excitation light is more efficiently absorbed, and saturation effects are more prominent.[25,61] In such case, saturation could be avoided under pulsed excitation at reduced power density, which led to higher S_r values compared to those obtained under continuous higher power excitation.[61] An additional advantage of reduced excitation power density is the lower risk of photo-induced damage to the sample under investigation.

In 2022, Yuan *et al.* capitalized on the 1210 nm excitation ability of Tm^{3+}.[59] They suggested co-doping with Er^{3+} ions and using the NIR-III emissions of Tm^{3+} at 1460 nm and Er^{3+} at 1525 nm, following a double-band ratiometric approach, to overcome the limitations encountered by use of the Tm^{3+} NIR-I emission. Higher resolution imaging at deeper penetration depths were demonstrated when using 1208 nm excitation *versus* 808 nm (Fig. 4A), in agreement with previous reports on the effect of excitation wavelength.[25,62] While a moderate maximum S_r value was obtained (0.36% K^{-1} at 293 K), the authors demonstrated the suitability of the developed NIR-II–NIR-III emitter for deep tissue thermal sensing in mice. It is important to note that even though the obtained S_r value can be considered relatively low for a double-band ratiometric approach, the proposed nanothermometer system was successfully applied in aqueous media, where surface and thermal quenching effects are heightened and can negatively impact thermal sensitivity. This work is in line with other studies that manifested the advantages of longer NIR wavelengths for biomedical applications.[63] Recent outstanding examples of nanothermometers operating in spectral region longer than 1000 nm will be showcased below, after providing some additional insight into recent achievements regarding Tm^{3+}-based nanothermometers of improved performance and for applications at temperatures beyond the physiological regime.

With respect to the latter, work by Runowski *et al.* is worth mentioning.[45] While well-known thermal quenching of the

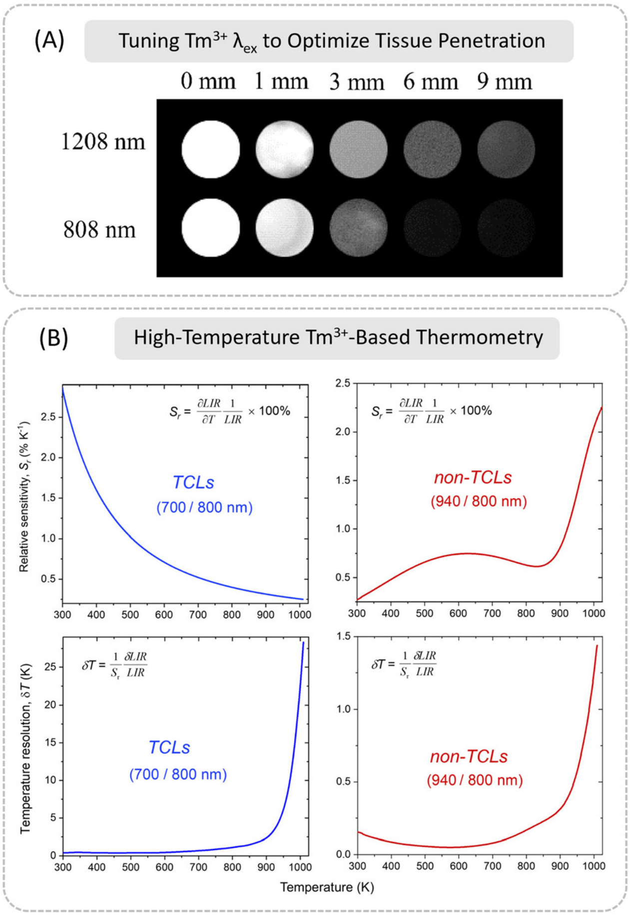

Fig. 4 Tuning the excitation and emission wavelengths of Tm^{3+}-doped nanothermometers towards biomedical and high-temperature applications – (A) *in vitro* assessment of the penetration depth of light emitted from $NaYF_4$:Tm^{3+},Er^{3+}@$NaYF_4$@SiO_2 under 1208 nm Tm^{3+}-excitation *versus* light emitted from $NaYF_4$:Ho^{3+},Yb^{3+}@$NaYF_4$:Nd^{3+}@SiO_2 under 808 nm Nd^{3+}-excitation (tissue: pork muscle). Overall stronger penetrability and lower tissue attenuation were observed under 1208 nm excitation. Reproduced from ref. 59 with permission from Elsevier, copyright 2022. (B) S_r and δT plots as a function of a wide temperature range spanning from 300–1000 K using the TCLs of the Tm^{3+} $^3F_3 \rightarrow {}^3H_6$ and $^3H_4 \rightarrow {}^3H_6$ transitions (700/800 nm) as well as the non-TCLs of the Yb^{3+} $^2F_{5/2} \rightarrow {}^2F_{7/2}$ and Tm^{3+} $^3H_4 \rightarrow {}^3H_6$ transitions (940/800 nm) following a LIR approach. Reproduced from ref. 45 with permission from American Chemical Society, copyright 2020.

Ln^{3+} emissions can hamper the application of Ln^{3+}-based nanothermometers at high temperatures,[64] the authors demonstrated how the NIR-I emission of Yb^{3+} and UC emission of Tm^{3+} can be used to provide a highly sensitive thermal readout at temperatures up to 1000 K. For the Yb^{3+}/Tm^{3+}-co-doped system, reduced thermal quenching effects were observed for Yb^{3+} when compared to the NIR-I upconverted emissions of Tm^{3+}. Due to the phonon-assisted thermalization of Yb^{3+}, higher thermal sensitivities were achieved at higher temperatures when using the LIR of the Yb^{3+} $^2F_{5/2} \rightarrow {}^2F_{7/2}$ and Tm^{3+} $^3H_4 \rightarrow {}^3H_6$ transitions (being non-TCLs). This contrasts with the TCLs of Tm^{3+} at 700 and 800 nm which were also explored, where thermal sensing capability was still maintained at higher temperatures, but temperature resolution decreased due to a poor signal-to-noise ratio resulting from emission intensity lost to thermal quenching of the Tm^{3+} UC emissions (Fig. 4B). The authors ensured thermal sensing at higher temperatures by choosing a heat-resistant host lattice, namely YVO_4, and by removing black body radiation generated from the thermalization of the emission bands through background corrections. Such nanothermometers are of particular interest for industrial applications, such as catalysis, high-temperature synthesis, and metallurgy, which require fast and reliable remote thermal monitoring at more extreme conditions.[45] Worth mentioning, the operational temperature regime of the developed nanothermometer was not limited to high temperatures, but when using the non-TCLs of Tm^{3+} and Yb^{3+}, also exhibited strong thermal sensitivity in the physiological temperature regime, allowing for potential use for a wide range of thermal sensing applications.

Towards deeper penetration depth and higher spatial resolution – nanothermometry in the NIR-II and -III windows

Seeking biomedical applications, such as deep-tissue optical imaging and thermal sensing at high spatial resolution, the ability of the applied light to penetrate the biological tissue is a key parameter. Challenges include absorption and scattering of light by water and biological tissues and components, *e.g.*, blood, haemoglobin, melanin, and lipids,[65] limiting penetration depth. Tissue auto-fluorescence can lead to the presence of unwanted background signals that reduce the brightness and contrast of the desired signals.[66,67] When scattering and autofluorescence of light occurs, tissue-induced light extinction can significantly compromise the spatial resolution of a nanothermometer, and parameters such as the signal-to-noise ratio and δT can be negatively impacted.[11,37,44,68] By shifting to longer wavelength in the NIR-II and -III regions (*ca.* 1000–1900 nm), the signal-to-noise ratio can be improved 100-fold due to reduced scattering of light and autofluorescence by biological tissues.[32] Notably, it has been observed that the contribution of NIR autofluorescence on *in vivo* bioimaging becomes almost negligible when using wavelengths longer than 1100 nm.[25,69] The use of longer wavelengths is also favourable as it can reach greater penetration depths into tissues, opening up the potential for better resolved deep optical imaging and *in vivo* applications.[38] In particular, the reduced scattering coefficient of wavelengths residing in the NIR-II region allow for deeper penetration depths to be achieved.[70] This has resulted in an increase of publications exploring Ln-NPs operating in the NIR-II and -III regions.[38] The development of more efficient and cheaper InGaAs detectors suitable for the wavelength region above 1000 nm likely contributed to this paradigm shift, demonstrating how the availability of new analytical devices goes hand in hand with probe development.[38] The most commonly explored Ln^{3+} ions with emissions at wavelengths longer than 1000 nm are Nd^{3+}, Ho^{3+}, Er^{3+}, and Tm^{3+}.[64,71] By co-doping with Yb^{3+} or Nd^{3+} as the sensitizer, the longer wavelength emissions generated can be used to quantify temperature following a double-band ratiometric approach. In recent years, research efforts have been dedicated to further improving the excellent thermal sensitivity of double-band nanothermometers by optimizing parameters such as host lattice phonon energy and NP architecture. Some of these examples will be outlined below.

Recent progress with double-band nanothermometers operating in the NIR-II/III

Er^{3+} is one of the most explored Ln^{3+} ions for thermal sensing in the NIR-III range based on its emission at 1550 nm ascribed to the ion's $^4I_{13/2} \rightarrow {}^4I_{15/2}$ transition. Since the first opening of the NIR-III window by Skripka *et al.* in 2017,[72] several luminescent nanothermometers have been reported using the 1550 nm emission of Er^{3+} together with the emissions of other Ln^{3+} ions, including Yb^{3+}, Ho^{3+}, Nd^{3+}, and Tm^{3+}.[17,73–76] Herein, the focus is often set on the optimization of S_r. For example, the combination of positive and negative thermal quenching effects has been verified as an effective strategy in that regard. In 2022, Wang *et al.* proposed a $Nd^{3+}/Yb^{3+}/Er^{3+}$ system with high S_r (3.1% K^{-1} at 293 K) by mixing two types of Ln-NPs, namely $NaNdF_4$:Yb@$NaYF_4$ (average size: 18 nm) and $NaErF_4$@$NaYF_4$ (average size: 34 nm) core/shell NPs.[73] Under 808 nm excitation of Nd^{3+}, with the rising of temperature, the Yb^{3+} emission intensity decreased (positive thermal quenching effect), while that of the Er^{3+} emission increased (negative thermal quenching effect). The opposite temperature-dependent emission intensity variation contributed the high S_r value of 3.1% K^{-1}. An even higher S_r value of 4.2% K^{-1} was obtained following a similar approach using $Sc_2Mo_3O_{12}$:Yb/Er and ZrO_2:Yb/Ho sub-micron sized powders.[77] While these studies demonstrated excellent thermal performance, the heterogeneity of the systems based on a physical mixture of two types of particles of different sizes and compositions may limit their practical application, *e.g.*, in biological environments due to the size-dependence of nano-bio interactions.[78]

Following seminal work that took advantage of host lattice phonons,[79] Jia *et al.* capitalized on this strategy and proposed a new type of phonon-based LIR thermometry.[74] The authors co-doped Yb^{3+}, Ho^{3+}, and Er^{3+} into various oxide NPs, *i.e.*, Gd_2O_3, Y_2O_3, $Y_3Al_5O_{12}$ (YAG), $BaTiO_3$ (BTO), and YVO_4, to investigate the effect of the phonon energy on the thermometric performance. They illustrated that multi-phonon relaxation (MPR) in Er^{3+} ions and phonon-assisted transfer processes (PAP) in Ho^{3+} ions played a significant role in LIR determination through channelling the harvested excitation energy to the corresponding emitting states (Fig. 5A). Herein, the dominant phonon energy of the host lattice, corresponding to the strongest peak in Raman and FT-IR spectra, contributed most to the MPR and PAT processes, and the S_r decreased with an increase of the dominant phonon energy. Despite of the highest S_r value (1.01% K^{-1} at 338 K) obtained in this work did not offer improvement of thermal sensitivity compared to the previously published work by Wortmann *et al.* on Ho/Er-doped $NaYF_4$ (2.15% K^{-1} at 310 K),[81] this approach provides a route to tune the sensing performance exploiting host phonons.

In 2024, Puccini *et al.* investigated the combination of Ho^{3+} with underexplored Pr^{3+} doped into core/multi-shell $NaGdF_4$ NPs for NIR-II double-band nanothermometry.[28] A maximum S_r value of 2.4% K^{-1} at 313 K was obtained for NPs dispersed in toluene. Quenching of the Ho^{3+} emission around 1180 nm when dispersing the Ln-NPs in water prevented their use as double-band thermometers in aqueous dispersions. Nonetheless, excellent single-band thermometric performance, using the Pr^{3+} emission at 1300 nm, was retained (*vide infra*).

An outstanding study among recent works demonstrating the promising temperature detection capability of NIR-II/III nanothermometers for biomedical applications was reported by Hu *et al.* in 2022.[80] Through the mindful design of a core/multi-shell architecture, the cross-relaxation processes of the host lattice ($NaGdF_4$) and Ln^{3+} dopants (Tm^{3+} and Nd^{3+}) were used to enhance the NIR emission intensities and in turn thermometric performance. Due to cross-relaxation processes between emitting Tm^{3+} ions and Gd^{3+} ions from the host material of the core, the quantum yield of the Tm^{3+} NIR-III emission (centred at 1470 nm) had a ~25-fold increase compared to doping Tm^{3+} ions into a $NaYF_4$ host lattice. By designing a core/multi-shell structure, comprising of a Yb^{3+}/Tm^{3+}-doped core, a first Yb^{3+}-doped shell, a second Yb^{3+}/Nd^{3+}-doped shell, and a third undoped shell, the intensity of the 1470 nm Tm^{3+} emission exhibited a 3.1-fold enhancement (Fig. 5B). By using this Tm^{3+} NIR-III emission alongside the Tm^{3+} NIR-II emission (centred at 1215 nm), under 808 nm excitation of Nd^{3+}, the authors successfully demonstrated *in vivo* temperature imaging in a mouse inflammation model following a double-band ratiometric approach. It should be noted that the 1470 nm Tm^{3+} emission is often defined as residing in the NIR-III region. However strictly speaking, due to water absorption (Fig. 1A/B), this emission falls between the BWs of the NIR-II and NIR-III region. Nonetheless, as already mentioned above, there is demonstrated relevance and suitability of this wavelength region for *in vivo* applications.

Highly noteworthy, Tm^{3+} recently attracted growing attention as an alternative NIR-III emitter because of its emission at 1800 nm ascribed to the ion's $^3F_4 \rightarrow {}^3H_6$ transition. It has been shown that wavelengths longer than 1500 nm not only provide deeper tissue penetration, but also exhibit better imaging contrast owing to extremely reduced light scattering.[30] In that regard, Ho^{3+} is another candidate of interest, given its 1960 nm emission stemming from the $^5I_7 \rightarrow {}^5I_8$ transition. Interestingly, Nexha *et al.* reported Tm^{3+}/Ho^{3+} co-doped $KLu(WO_4)_2$ NPs as NIR-III thermometers, taking advantage of the 1800 nm Tm^{3+} and the 1960 nm Ho^{3+} emission bands under 808 nm excitation of Tm^{3+} (Fig. 5C).[23] The temperature-dependent performance of the probes was governed by energy transfer and back-energy transfer processes between the $^3F_4$ level of Tm^{3+} and the $^5I_7$ level of Ho^{3+}. The highest S_r value (0.9% K^{-1}

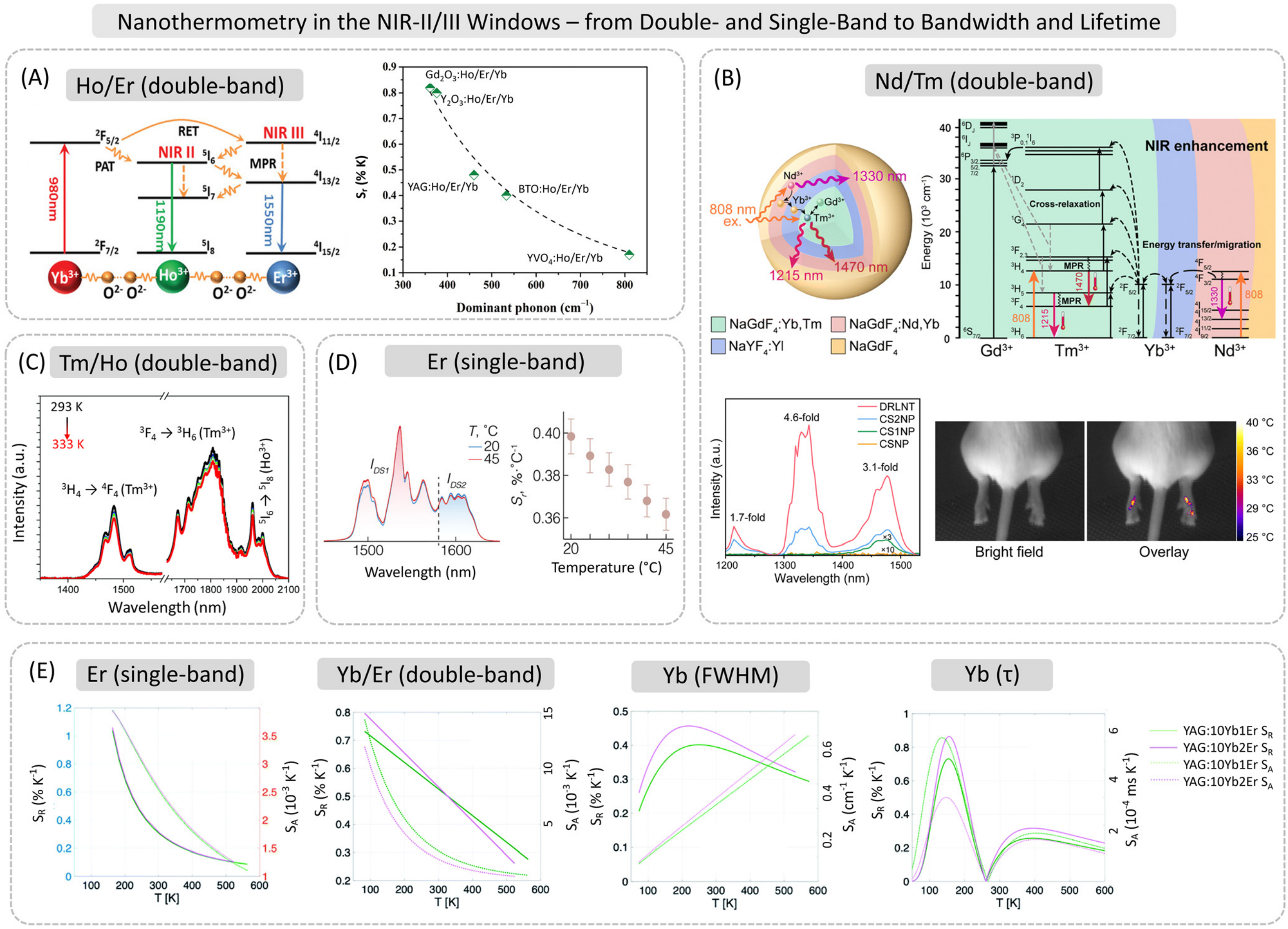

Fig. 5 Recent trends in nanothermometry in the NIR-II/III spectral region – (A) phonon-based LIR mechanism (left) and the calculated S_r values at 573 K *versus* dominant phonon bands of various oxide host lattices (right) in Ho/Er based double-band nanothermometers. Reproduced from ref. 74 with permission from Wiley, copyright 2020. (B) Example of a Nd/Tm-based double-band nanothermometer for *in vivo* applications: (top) Schematic of the $NaGdF_4$:Yb,Tm@$NaYF_4$:Yb@$NaGdF_4$:Yb,Nd@$NaGdF_4$ core/multi-shell architecture (DRLNT) and its corresponding energy diagram; (bottom) NIR luminescent spectra of the Ln-NPs of different compositions, and the demonstration of *in vivo* thermal imaging using DRLNT NPs in a mouse inflammation model. The right hind paw was injected with carrageenan to induce inflammation. The left paw was injected with saline as a control. Reproduced from ref. 80 with permission from Royal Society of Chemistry, copyright 2022. (C) Towards longer emission wavelengths: temperature-dependent emission of a Tm/Ho-based double-band nanothermometer (host: $KLu(WO_4)_2$). Reproduced from ref. 23 with permission from Royal Society of Chemistry, copyright 2020. (D) Er-based single-band nanothermometry: Temperature-dependent emission spectra of Er^{3+} and the corresponding S_r values for $LiErF_4/LiYF_4$ NPs in aqueous suspension. Reproduced from ref. 26 with permission from Wiley, copyright 2020. (E) Four temperature readout approaches (Er single-band, Yb/Er double-band, full width half maximum (FWHM), and lifetime of Yb) reported in Yb/Er doped YAG NPs. Reproduced from ref. 46 with permission from Royal Society of Chemistry, copyright 2021.

at 293 K) was obtained based on the ratio of I_{1800}/I_{1960}. This work constitutes the first report exploring nanothermometry in the wavelength range from 1800 to 2000 nm, opening the path to nanothermometry at very longer NIR wavelength regions.

Overcoming limitations to *in vivo* temperature sensing

Regardless of the clear advantages of longer wavelengths, there are still several limitations regarding the implementation of nanothermometers in biomedical applications that the community has been working on to address. Factors such as the aforementioned tissue penetration depth can influence how much light reaches the nanothermometer and how accurately the emission can be recorded with sufficient enough signal-to-noise ratios required to produce a reliable thermal readout. Shifting to longer wavelengths allows for greater penetration depths into tissues as well as reduced tissue autofluorescence, however, soluble components present in intra- and extra-cellular environments can produce light scattering that can compromise the accuracy of a nanothermometer. Therefore, care must be taken when considering a nanothermometer for *in vivo* studies as different tissues will have different attenuation to light and in turn can alter the spectral shape of the emissions, causing error in thermal readout. The reader is guided to the recent work of Shen *et al.*, where this effect is demonstrated in detail.[44] As briefly introduced in previous sections, a popular solution to this is the development of single-band nanothermometers, where the LIR between bands stemming from the emission of a single NIR region is less affected by heterogeneous attenuation. Another common limitation identified when considering *in vivo* application is the need to recalibrate the nanothermometer systems. In many studies, the calibration of the intensity ratio (LIR *versus* T plot) is performed in colloidal dispersions in a cuvette and not *in situ*. Therefore, the performance of the nanothermometer is not calibrated to the true experimental environment and the resulting thermal readout cannot be trusted. Again, it has been seen that single-band nanothermometers based on TCLs that follow a Boltzmann distribution result in more consistent calibration curves in different solvents and environments.[82] Recent reports of single-band nanothermometers operating at longer emission wavelengths will be highlighted below. The use of lifetime-based approaches to thermal sensing have also proven useful in minimizing calibration curve inconsistencies and will be described in the following section. For a more comprehensive overview of the limitations and challenges often encountered when proposing nanothermometers for biomedical applications, the reader is guided to the critical work by Labrador-Paez *et al.*,[20,83] as well as reviews by Quintanilla *et al.*[11] and Bednarkiewicz *et al.*[37]

Establishing single-band nanothermometry in the NIR-II/III

While the Stark sublevels of the NIR-I and -II emissions of Nd^{3+} and the NIR-I emission of Tm^{3+} have been widely investigated as single-band NIR-NIR nanothermometers,[22,24,25,42] the first report of Er^{3+} single-band nanothermometry operating at longer wavelengths was published in 2020 by Hazra *et al.*[26] The authors demonstrated the suitability of Er^{3+} in $LiErF_4$/$LiYF_4$ NPs for single-band thermometry based on the Stark splitting of the Er^{3+} $^4I_{13/2}$ and $^4I_{15/2}$ manifolds (centered at 1550 nm) into Boltzmann-coupled sublevels. As shown in Fig. 5D, under 793 nm excitation, elevating the temperature in the physiological temperature range (20–45 °C), an isothermal point around 1580 nm could be discerned in the intensity normalized downshifting spectra. The LIR thermometric parameter $\Delta_{DS} = I_{DS1}/I_{DS2}$ was defined between two integration ranges, I_{DS1} (1450–1580 nm) and I_{DS2} (1580–1650 nm), resulting in a maximum S_r value of 0.4% K^{-1} at 293 K in aqueous suspension. Considering its performance in aqueous suspension, this stands as the best performing Er^{3+} NIR-III single-band nanothermometer operating in the physiological regime reported to date.

Following previous work on Er^{3+} single-band nanothermometers,[26,84] in 2021, Perisa *et al.* investigated the thermal dependence of the Er^{3+} NIR-III emission in a Yb^{3+}/Er^{3+}-doped YAG NP system following four different thermometric approaches (Fig. 5E).[46] They observed that thermal sensitivity is highly dependent on the explored temperature range. When following a Boltzmann governed approach using the Stark sublevels of the Er^{3+} $^4I_{13/2}$ and $^4I_{15/2}$ manifolds as well as the LIR approach using the distinct Er^{3+} and Yb^{3+} NIR emissions, maximum S_r values can be obtained when sensing at lower temperature regimes (1% K^{-1} at 163 K and 0.8% K^{-1} at 83 K, respectively), compared to physiological temperatures (0.3% K^{-1} and 0.5% K^{-1} at 310 K, respectively). Considering a bandwidth change approach to thermal sensing based on the Yb^{3+} $^2F_{5/2} \rightarrow {}^2F_{7/2}$ transition, S_r values remained fairly consistent over the investigated temperature range (80–600 K), with S_r values in the physiological range being comparable to reports of other Er^{3+}/Yb^{3+}-doped nanothermometers that follow a bandshift approach.[85] Finally, they employed a lifetime-based approach using the Yb^{3+} emission, where thermal performance was observed better at temperatures below the physiological range. The good thermal sensitivities realized at low temperatures open up possibilities for reliable thermal sensing in environments compromised by visible background absorption and scattering as well as extend the application of nanothermometry outside the field of life sciences.

Recently, Puccini *et al.* suggested for the first time the use of the Pr^{3+} emission centred at *ca.* 1300 nm (ascribed to the $^1G_4 \rightarrow {}^3H_5$ transition) for NIR-NIR thermal sensing in aqueous dispersions following a single-band ratiometric approach.[28] Through core/shell architectural design and excitation power optimization the authors achieved an unprecedently high S_r value of 0.8% K^{-1} at 283 K. Despite the use of 980 nm for excitation, laser-induced heating effects were minimized at power densities as low as 2.47 W cm^{-2}. Of interest with respect to real-life application, such low laser power density fostered higher thermal sensitivity, as also observed by Marciniak *et al.*[61] This work also constitutes an example for thermal sensing optimization through architectural design. While additional co-doping with Ho^{3+} added capability for double-band nanothermometry (*vide supra*), the spatial separation of the Pr^{3+} ions from the Ho^{3+} ions by core/multi-shell design was strictly necessary for the single-band approach based on Pr^{3+}.

Beyond ratiometric thermal sensing: lifetime-based nanothermometry

When designing nanothermometers for life science applications, consideration must be placed on how the biological media, such as the tissue of an organism, affect the optical properties of Ln^{3+} dopants. The emission intensity approach (based on the LIR) to thermal sensing is most commonly employed, however, emission intensities used to quantify the thermometric performance can be highly dependent on the physical and chemical environment.[37] For instance, parameters such as the presence of ligands and molecules, as well as viscosity and pH of the surrounding media may affect emission intensity and lead to inaccurate thermal readouts. To overcome these limitations, a lifetime-based approach to thermal sensing has been proposed. Lifetime-based nanothermometers are advantageous in that their optical properties are less affected by the surrounding environment, concentration of the probe, and excitation intensity.[86] Despite the widely established knowledge about the advantages of lifetime over intensity, for instance in bioimaging,[87] there appears to be a gap in research concerning the development and application of lifetime-based nanothermometers operating in the NIR region. This may be due to the higher complexity of the experimental setup needed for time-resolved spectroscopy. It has been observed that the multi-phonon relaxations of Ln^{3+} ions are enhanced at higher temperatures, thus, resulting in shorter lifetime. This relationship between temperature and lifetime allows for thermometric performance to be quantified. First proposed in the 1980s as a "decay time temperature sensor"[88] and with seminal advancements arising in the early 2000s on UC lifetime-based nanothermometers,[89,90] there have been several reports of Ln^{3+}-doped lifetime-based nanothermometers comprised of a wide variety of host materials operating across all regions of light. For instance, lifetime-based nanothermometers using the NIR-I emission of Tm^{3+} and Yb^{3+}, the NIR-I and -II emissions of Nd^{3+}, and the NIR-II emission of Ho^{3+} have been reported.[47–50,91–93] Owing to the ability to use excitation and emission wavelengths matching the optical transparency windows, lifetime-based nanothermometers are often multimodal, and have been successfully employed as probes for *in vitro* and *in vivo* bioimaging in addition to thermal sensing.

Among recent achievements, in 2020, Tan *et al.* reported a $NaYF_4{:}Yb^{3+},Nd^{3+}$ lifetime-based nanothermometer operating in the NIR-I region.[49] By using the lifetime of the $^2F_{5/2} \rightarrow {}^2F_{7/2}$ transition of Yb^{3+} (980 nm), the emission of which was facilitated by energy transfer from sensitizing Nd^{3+}, S_r values up to 1.4% K^{-1} were achieved over the physiological temperature range in aqueous dispersions. Through a considerate multi-shell architecture design, the authors were able to resolve temperature changes in tissue depths up to 4 mm. To pose their nanothermometer system for *in vivo* applications, minimal laser heating effects and no dependence on Ln-NP concentration or environmental pH were reported. By injecting the nanothermometers into mice, thermographic luminescence lifetime-hued imaging was performed to accurately map the temperature distribution of inflammation within the mice (Fig. 6A). Following these findings, Kong *et al.* applied a

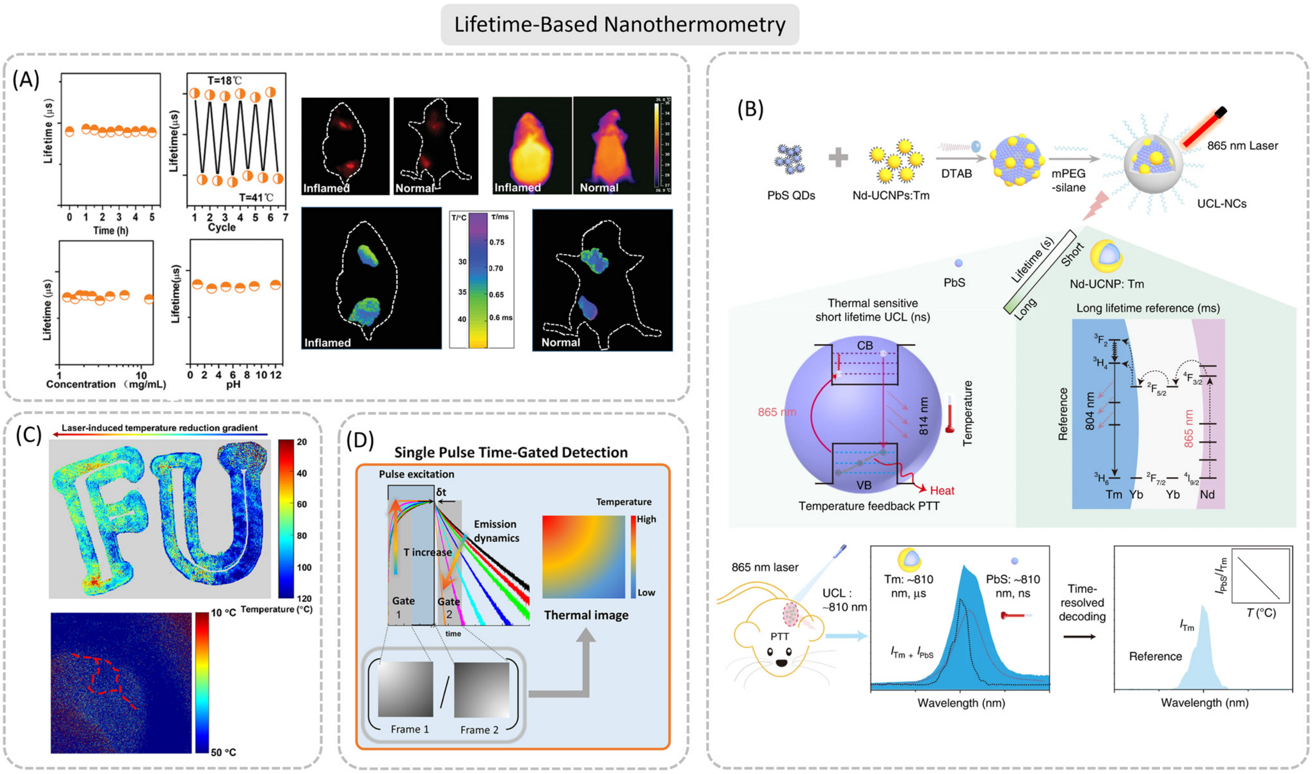

Fig. 6 Lifetime-based approaches to *in vivo* temperature sensing – (A) (left) Lifetime of the $^2F_{5/2} \rightarrow {}^2F_{7/2}$ transition of Yb^{3+} from $NaYF_4@NaYF_4{:}Yb^{3+},Nd^{3+}@CaF_2$ NPs as a function of intense 800 nm laser exposure over 5 h at constant temperature, over 5 heating and cooling cycles (repeatability R), Ln-NP concentration, and pH at constant temperature. (right) Thermographic luminescence lifetime-hued imaging of a living mouse showing precise local temperature detection of inflamed *versus* normal tissue. Reproduced from ref. 49 with permission from Wiley, copyright 2020. (B) Schematic of the workflow and design of a hybrid PbS quantum dot (QD)/Tm-NP system exhibiting the same emission wavelength (*i.e.*, 810 nm) under 865 nm laser excitation. The temperature sensitive short lifetime generated from the Tm-NPs was used with the referencing long lifetime obtained from PbS to provide reliable *in vivo* thermal readout following a time-resolved technique. Reproduced from ref. 94 with permission from Springer Nature, copyright 2020. (C) *In vitro* and *in vivo* temperature mapping of "FU" and a mouse leg blood vessel following a frequency-domain lifetime imaging approach using the Yb^{3+} emission from β-$NaNdF_4{:}7\%Yb,33\%Y@NaYF_4@NaYbF_4{:}2\%Er,2\%Ce@NaYF_4$ NPs. Reproduced from ref. 50 with permission from American Chemical Society, copyright 2023. (D) Schematic of the workflow of real-time thermal imaging using single-pulse time-gated detection. Reproduced from ref. 96 with permission from Wiley, copyright 2022.

similar system for vascular temperature mapping of living mice.[48] This report stands as the first endeavour of minimally invasive thermal mapping of vessels with NIR emitting nanothermometer, and alongside the work from Tan *et al.*, prove to be a large step in *in vivo* applications of NIR-to-NIR nanothermometry. As an alternative to Nd^{3+}, Raab *et al.* proposed a single-band lifetime-based nanothermometer using 976 nm excited Yb^{3+}/Tm^{3+} co-doped $NaYF_4$ NPs, also operating in the NIR-I region.[47] No *in vitro* or *in vivo* studies were included, but the thermometric performance in aqueous dispersion over the physiological temperature range was evaluated with a maximum S_r of 0.92% K^{-1}. However, prior to this, in 2020, Qiu *et al.* proposed a way to avoid use of 980 nm excitation sources by adding a sensitizing Nd^{3+}-doped shell onto their Tm^{3+}/Yb^{3+}-doped core-shell NPs.[94] With an attempt to improve the thermal sensitivity, a hybrid structure combing Tm^{3+}/Yb^{3+}-doped NPs with PbS quantum dots was designed (Fig. 6B). When excited with 865 nm light, both the PbS QD and Tm^{3+}-doped NPs exhibited emission at the same NIR-I wavelength, however, their temperature-dependent lifetimes were different. This allowed for a dual ratiometric approach to thermal sensing *via* time-resolved decoding. Moreover, the error associated with using emissions of different wavelengths in different NIR regions was minimized. Following an *in vitro* study to evaluate the effect of tissue thickness on thermal sensing abilities, a S_r value of 5.6% K^{-1} at 318 K was maintained at tissue depths up to 3 mm. Qiu *et al.* also tested their hybrid nanothermometer in an *in vivo* experiment, in which temperature feedback photothermal therapy was successfully performed on tumour bearing mice. Reports of lifetime-based nanothermometers taking advantage of the NIR-III emission of Er^{3+} are scarce, but this phenomenon was recently explored in the work by Balabhadra *et al.*[95] The authors reported an unprecedently high S_r value of 1.32% K^{-1}, however, this was at low temperatures (150 K), and thermal performance was seen to decrease with an increase in temperature. Moreover, visible excitation at 523 nm was performed to generate emission from the Er^{3+} $^4I_{13/2}$ manifold, instead of commonly used NIR excitation, limiting the application of this system as a NIR–NIR nanothermometer. Nonetheless, to the best of our knowledge, this study stands as the only report of Er^{3+}-doped lifetime-based nanothermometry and opens the field for further exploration. Regardless, co-doping with Er^{3+} has shown potential when creating multimodal probes for simultaneous bioimaging and temperature mapping. In 2023, Sun *et al.* designed a multilayer nanoprobe capable of simultaneously detecting temperature in the NIR-I region and providing high-resolution imaging in the NIR-III region.[50] The Nd^{3+} sensitized NIR-I emission of Yb^{3+} was used to undergo a lifetime-based thermal sensing approach demonstrated through *in vitro* temperature detection. The authors concluded that the external solvent environment does not influence thermometric performance when a lifetime-based approach was used and obtained a maximum S_r value of 1.94% K^{-1} at 298 K. By co-doping with the NIR-III emitter Er^{3+}, through a multilayer design, *in vivo* frequency-domain lifetime-based imaging with simultaneous temperature mapping of mice blood vessels was successfully performed (Fig. 6C). This serves as strong step forward towards the design and practical application of dual-function NIR-NIR Ln-doped nanoprobes capable of simultaneous temperature detection and bioimaging.

Temporal resolution is a key parameter for dynamic real-life applications such as *in vivo* thermal imaging. For optical probes with rather long lifetimes, as it is often the case for NIR-emitting Ln^{3+}, thermal imaging can be achieved using a time-gated camera that is correlated with a modulated pulse excitation source. However, this can lead to relatively long acquisition times, preventing real-time thermal sensing.[96] Addressing this drawback, Avram *et al.* developed a single-pulse time-gated detection method (Fig. 6D).[96] Processing times in the range of 1–10 ms were achieved, enabling real-time lifetime-based thermal imaging.[96] In addition, using the NIR-II emission of Ho^{3+} in two different host materials, *i.e.*, Y_2O_3 and β-$NaYF_4$, a maximum S_r value of 0.93% K^{-1} at 330 K for the Y_2O_3 NP system was achieved in aqueous media. By comparing the performance of their lifetime-based nanothermometer following the single-pulse method with the average lifetime method used by other groups, they observed an increase in thermal sensitivity, with the S_r value at 330 K increasing to 0.93% K^{-1} from 0.2% K^{-1}. Of promise regarding real-life implementation is the demonstrated single-pulse time-gated thermal imaging using an accurate lifetime-based temperature readout method enabling shorter processing time (<10 ms) for real-time temperature measurements and reduced equipment costs due to the use of a lower frame rate (<100 Hz) for biological applications. This work clearly stands out as in-depth optimization of parameters such as time delay, gate, and acquisition time are not regularly considered. Likewise, temporal resolution is another parameter that future research must address in more detail to bring lifetime-based thermal sensing and imaging into real-life *in vivo* applications.

The role of the host material

The effect of host material, particularly regarding host phonon energy and crystal coordination environment, on the thermometric performance of a nanothermometer system has been widely studied. The bulk of reports focuses on how tailoring the choice of inorganic host material enhances the thermal sensing abilities of UC-based nanothermometers.[39,97] Using the same design principles, recent efforts have outlined similar effects for NIR-emitting nanoprobes.[66,98–100] Generally, host materials with low phonon energy reduce non-radiative losses, in turn boosting optical properties, primarily the UC quantum yield. Moreover, host materials with stronger crystal fields enhance the absorption and emission of Ln^{3+} ions.[100] However, the choice of host material has been observed to influence the thermal sensitivity following mechanisms and relationships different to those used to enhance emission intensity, brightness, and quantum yield. For example, host materials with low phonon energy, such as fluorides, are useful in extending the temperature sensing range. Herein, the probability of non-radiative depopulation is reduced, allowing for sufficient population of the emitting level even at lower temperatures.[101] As well, as mentioned above with reference to work by Jia *et al.*, the S_r value can increase with a decrease in dominant phonon energy of the host material.[74] In contrast, in host materials with higher phonon energy, such as oxides and oxyfluorides, the probability of non-radiative relaxation processes increases. Though this can have a negative effect on the overall emission intensity, it has also been proven advantageous for thermal sensing.[102–104] In particular, the work by Savchuk *et al.* demonstrated the influence of host material on the brightness and thermometric performance of the NIR-III emission of Er^{3+} following a single-band approach.[102] The host material with the lowest phonon energy, $NaYF_4$, produced the brightest emission, yet resulted in the lowest S_r value among the investigated host materials. A host material with higher phonon energy, *i.e.*, oxyfluoride NaY_2F_5O, exhibited a three times greater S_r value than $NaYF_4$. This effect was also demonstrated by Suo *et al.*[105] This study established a correlation between host material phonon energy, bond covalency, and absolute thermal sensitivity for nanothermometers based on the UC emissions of Er^{3+} and Yb^{3+}. The increase in both host phonon energy and bond covalency when using oxides over fluorides led to a 4-fold increase in thermal sensitivity. The authors also investigated the effect of local symmetry of the host lattice on the absolute thermal sensitivity, concluding that the strong local site symmetric distortion induced by the ionic radius mismatch between dopants and host cations led to enhanced thermal sensitivity and signal-to-noise ratio.[106] Direct excitation of the host material is an alternative approach to enhance S_r. Herein, host-to-dopant phonon-assisted energy transfer allows for the excitation of the emitting Ln^{3+} ions, as demonstrated for Ln^{3+}-doped YVO_4.[98] However, this strategy requires UV excitation.

Optimization of the host material also plays a significant role for single-band nanothermometry. As mentioned above, the S_r value is directly proportional to the ΔE of the thermally coupled emitting levels. Depending on the host material that the Ln^{3+} ions are doped into, the ΔE of the emitting level can increase or decrease following phonon-assisted energy transfer. In principle, employing host lattices with greater phonon energy can be beneficial in increasing the ΔE of the emitting level, and in turn the S_r value. As well, by modifying the local crystal field around the emitting ion, a larger degree of Stark splitting can be induced for the TCLs, in turn enhancing the S_r value.[39,42] Choosing a host lattice that permits for well-resolved Stark splitting is ideal for clear identification of the sub-levels and emission wavelengths to be used for thermal sensing.[26] This was demonstrated in the work by Hazra *et al.*, in which a $LiYF_4$ host lattice was chosen for better resolution of the Stark sublevels of the Er^{3+} NIR-III emission for single-band ratiometric nanothermometry.

Still, the optimization of the host material is but one of the methods commonly used to enhance thermometric performance of NIR-NIR Ln^{3+}-based nanothermometers. Overall, the spectral features of the Ln^{3+} ions themselves endow Ln-NPs with thermal sensing abilities due to temperature-governed population or repopulation of the emitting energy levels, whose temperature-dependent changes are used to quantify a thermal readout. As discussed throughout this review, thermal sensitivity is affected by ion dopant concentration,[42] NP size and architecture,[28,73,77,80] excitation source and power density,[24,25,43,51,59] and of course Ln^{3+} ion type. Therefore, thoughtful, and strategic experimental methodology must be employed when considering the development of highly sensitive NIR nanothermometers.

Future directions

Recent advances of Ln^{3+}-doped NIR-NIR nanothermometers strongly focus on the optimization of conventional approaches, such as the double- and single-band LIR approaches. Regardless, there are still limitations and challenges that need to be addressed to allow for successful real-life implementation of nanothermometry into all potential applications. By combining alternative disciplines with the existing knowledge of nanothermometry, new approaches to luminescence thermal sensing can be developed with hopes of overcoming the remaining challenges while maintaining high thermal sensitivity and resolution. In light of this, some unconventional approaches are showcased that hopefully can help advance the field to new heights.

Luminescence intensity ratio squared (LIR^2)

While significant efforts were made over the last decade to increase the thermal performance, the relative low S_r values obtained from LIR-based nanothermometers operating in the NIR regions still limit their applications. Addressing this challenge, Ćirić *et al.* proposed a novel approach called luminescence intensity ratio squared (LIR^2) to enhance the S_r value.[27] This approach combines dual-excitation single-emission band ratiometric and conventional (Boltzmann) LIR techniques. As schematically shown in Fig. 2D, this approach involves two sets of TCLs, coming from a sensitizer and an activator ion, respectively. Due to the TCLs in the sensitizer ion, two excitation wavelengths can be used to trigger the emission from the activator ion. Hence, LIR^2 is determined by the ratio of emission intensities, which are excited under different wavelengths. The LIR^2 approach was first applied to NIR nanothermometry using $Y_3Al_5O_{12}$:Er^{3+},Yb^{3+} NPs as a model system. As the Stark sublevels of the $^2F_{7/2}$ ground state of Yb^{3+} were found to be thermally coupled, the two excitation wavelengths were determined at 916 nm and 1031 nm by measuring the temperature-dependent excitation spectra of Yb^{3+}. On the other hand, the Stark sublevels of $^4I_{13/2}$ of Er^{3+} were also thermally coupled. LIR^2 was determined using the ratio between the integrated emission intensities of Er^{3+} (I_1 = 1350–1500 nm as well as I_2 = 1500–1550 nm) under excitation at 916 and 1031 nm. The S_r value obtained based on LIR^2 was two-fold (0.9% K^{-1}) compared to that obtained by the LIR approach (0.4% K^{-1}), showing great promise for future applications. A limitation of the novel LIR^2 approach might, though, be the necessity of using two excitation wavelengths, thus, practical implementation requires a slightly more complex spectroscopic setup. An alternative double-excitation based nanothermometry was reported in Yb^{3+}/Nd^{3+} doped NaYF$_4$ particles under 980 nm and 808 nm excitations.[107] Xu *et al.* demonstrated that this self-reference thermometer had a very high S_r value (2.2% K^{-1}) and exhibited good immunity to the influences arising from the fluctuation and loss of pumping sources as well as the luminescence attenuation in media.

Improving thermal resolution

δT estimates the statistical uncertainty (precision) of the thermometric approach of interest. Since it may perform differently for different setups and acquisition conditions, a trial-and-error approach is usually used to identify the parameter that is most sensitive towards temperature. Moreover, it becomes more complicated when more than one thermometric approach based on the temperature-dependent spectroscopic features of the nanothermometer are used to quantify a thermal readout. Since δT is heavily dependent on experimental setup, the precision acquired following a lifetime-based approach may be different than the precision acquired following a LIR or bandshift approach. To address these challenges, in 2023, Ximendes *et al.* introduced a computational approach called dimensionality reduction (DR) technique to optimize the δT value.[68] LiErF$_4$@LiYF$_4$:Yb@LiYF$_4$:Yb@LiYF$_4$ NPs were chosen as a modal system for NIR-III nanothermometry, using the 1550 nm Er^{3+} emission. As a key finding, this unconventional approach led to improved thermal resolution (0.09 K) compared to the more classical intensity-based and ratiometric approaches (0.3 K). The authors further extended this data treatment to datasets gathered for the temperature-dependent NIR emission of Ag$_2$S semiconductor nanocrystals, confirming the general applicability of the proposed methods. Following this first demonstration, other researchers followed a similar strategy. As such, Soares *et al.* utilized this technique to determine the δT value (below 1 K) for a Tm^{3+}/Er^{3+}-based nanothermometer operating in the wavelength range from 1500 to 1800 nm.[108] The authors also illustrated that luminescence spectra acquired in the third biological window were minimally distorted by the presence of tissue, paving the way to more reliable luminescence thermometry.

Into the future: combining nanothermometry with machine learning

With the advent of computational and machine learning approaches for light matter interactions,[109] also nanothermometry is expected to undergo significant changes on how we approach it. First examples have demonstrated that machine learning can be applied in nanothermometry.[110–112] In early 2023, Stone *et al.* reported how the use of machine learning can address limitations with respect to calibration of a thermal sensor based on fluorescent nanodiamonds.[110] With the goal to determine the best combination of observable features and, simultaneously, the smallest number of calibration temperatures, one can rely on to determine the temperature, the authors trained a machine learning, multi-feature regression algorithm to produce a model that can predict the temperature of any other diamond nanosensor with 1.5 K accuracy. Shortly after this seminal example exploiting nanodiamonds, progress was also made in the field of Ln-based nanothermometers. Liang *et al.* demonstrated a self-optimization procedure to automatically identify the best LIR for temperature sensing based on a single Er-chloride-silicate nanowire operating in the 1500–1800 nm spectral range.[111] The authors reported record-breaking S_r values higher than 100% K^{-1} and a very large operations range from 4–500 K. Little later, Santos *et al.* developed an automated machine learning tool to select best

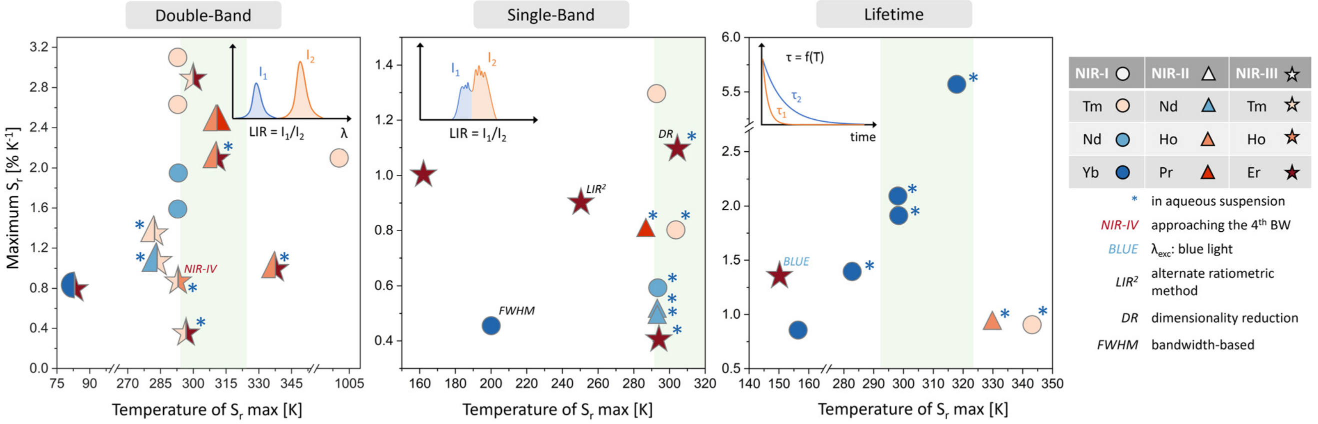

Fig. 7 Overview of reported maximum S_r values and the temperature [in K] that they were obtained at for the discussed NIR-NIR Ln-based nanothermometers following a double-band ratiometric approach (based on data from ref. 18, 23, 24, 28, 42, 43, 45, 46, 59, 72, 80 and 81), a single-band ratiometric approach (based on data from ref. 22, 24–28, 46 and 68), and a lifetime-based approach (based on data from ref. 46–48, 50, 94–96 and 113) to thermal sensing. Unconventional approaches such as LIR^2, dimensionality reduction as well as FWHM-based methods are also included and labelled accordingly. The green shaded region represents the physiological temperature range.

models capable to improve the accuracy of luminescent nanothermometers.[112] Herein, the emission of Nd^{3+} doped into YAG NPs was chosen as proof-of-concept, while the authors highlight that the approach can be extended to any photoluminescent material, also making an open-source code available to the broader community.

Concluding remarks

In conclusion, undoubtedly, significant advancements were made over the past years, resulting in more sensitive and reliable Ln^{3+}-based nanothermometers that use both excitation and emission wavelengths in the NIR region (Fig. 7). Seeking more robust thermometers for real-life application, limitations associated with excitation wavelength, the use of TCLs *versus* NTCLs, the need to recalibrate, and potential heterogenous attenuation from tissues were identified, and the benefits of shifting from an established double-band to a more reliable single-band ratiometric approach was successfully applied as a strategy to overcome some of these limitations. A growing number of studies demonstrates the benefits that arise from thermometric approaches based on lifetime and bandshift as alternative to LIR approaches, as well as novel unconventional methods to thermal sensing, including the LIR^2 method, and most recently, the combination of nanothermometry with machine learning.

To place Ln-NPs into the context of the diverse landscape of nanothermometers, also other material classes, including semiconductor quantum dots (QDs), metal nanoclusters (NCs), transition-metal (TM)-based NPs, polymers, and organic fluorophores, must be considered. To date, Ln-NPs and QDs (more specifically QDs based on Ag_2S) have become the candidates of choice when developing nanothermometers for *in vivo* applications due to their ability to absorb and emit in the BWs.[114] Most QDs possess excellent photostability allowing for prolonged excitation, as well as produce high quantum yields with bright emission intensities.[38,114] However, they may suffer from instability in intracellular environments, potentially resulting in non-homogenous luminescence.[38,115] Another drawback of traditional semiconductor QDs comprising of heavy metals (*e.g.*, Cd, Te, Se, and Pb) is their toxicity and the requirement for UV excitation, limiting their use for biological applications. Recent research efforts have been put on developing a new generation of QDs composed of non-toxic elements to permit the *in vivo* application of these materials. These include, for example, Ag_2S, $CuInS_2$, carbon-based, and Si QDs.[116–119] Yet, despite high promise, also QDs are potentially prone to bias, as recently highlighted by Ogáyar *et al.*[120] Metal nanoclusters, primarily based on gold (Au NCs), are appealing for *in vivo* thermal sensing applications due to their sub-2 nm sizes and good chemical stability and biocompatibility. Still, some drawbacks must be addressed such as concentration and surface quenching effects that may affect their performance.[114] TM-based NPs (TM: Ni, Mn, Co, Fe, V, and Cr) have gained much attention as being promising candidates for thermal sensing due to their high resistance to photobleaching and broad emission bands located in the visible to NIR-II region, but their need, similar to Au NCs, for UV-visible excitation renders them less attractive for biological applications.[121] In that regard, the combination of TM ions with Ln^{3+} ions, co-doped into an inorganic host lattice constitutes an interesting alternative, as demonstrated for, *e.g.*, Mn^{5+}/Er^{3+} co-doped $Ba_3(VO_4)_2$ showing strong, near-infrared emission and long, temperature-dependent photoluminescence lifetime.[122] Last but not least, research has evolved over the years yielding organic fluorophores and dyes with bright and stable luminescence intensities that can be easily incorporated into living cells. Still, their spectral properties are strongly environment-dependent, increasing the need for recalibration of the thermometer when placed in different media.[114]

Thus, particularly when aiming for *in vivo* thermal sensing applications, Ln-NPs can be considered as highly promising candidates. Their ability to generate deep-tissue penetrating NIR light, using low-cost NIR excitation sources, along with photostability, limited autofluorescence, and low toxicity, according to current knowledge, result in high thermal sensitivity and signal-to-noise ratios. In addition, the UC emission that is often observed in parallel to NIR emission or the magnetic properties of Ln^{3+} ions such as Gd^{3+} and Dy^{3+} bring multifunctionality to the scene, allowing for theranostics or multimodal imaging in addition to thermal sensing.[123,124]

Despite all promise, Ln-NPs possess their own set of challenges, often not much different to those faced by other materials classes, that dictate their performance and applicability for thermal sensing across a wide range of applications. Though efforts have been made to address several crucial challenges (*e.g.*, wavelength choices matching the biological windows for deeper penetration depth, higher resolution, and minimized spectral distortion by biological tissues; use of lifetime-based approaches to reduce the effect of laser power density; design of brighter core/(multi-)shell NPs leading to enhanced S_r and δT), there are still key limitations that impede the implementation of Ln^{3+}-based NIR-NIR nanothermometers to real-life applications:

- Notably, issues regarding batch-to-batch reproducibility and the overall reliability of nanothermometers over time remain. When considering real-life applications in the life sciences, surface functionalization needed to render NPs water dispersible often hamper brightness through both photonic and surface quenching effects, which in turn affects thermal readout. Therefore, optimization of surface chemistry needs to be addressed.

- There is also a need for the development of synthesis techniques that produce more homogenous, monodispersed, and colloidally stable Ln-NPs, as size and morphology can influence thermometric performance. Particularly, while synthesis methods towards alkali metal lanthanide tetrafluoride NPs of controllable size and morphology have advanced over the past two decades, there still is a need for control of size and morphology at the nanoscale of other promising host materials, such as oxides, phosphates, or tungstates.

- With the recognition that longer wavelengths are more suitable for application in biological environments, wavelengths matching the fourth near-infrared window (NIR-IV) reaching into the spectral region beyond 2000 nm have shown promising results for bioimaging applications.[30] Hence, while first nanothermometers that operate at 1800–1960 nm have been demonstrated, the NIR-IV window remains to be fully opened for the field of nanothermometry.
- The latter might be a challenge as even NIR-III-based nanothermometers that operate at the physiologically relevant temperature range remain scarce. Summarizing recent achievement (Fig. 7), the majority of probes that exhibit relatively high S_r values are still based in the NIR-I spectral region, with only a few exceptions. Noteworthy, lifetime-based nanothermometers have resulted in excellent S_r values outperforming those based on single- or double-band approaches. Still, a shift towards longer wavelengths remains to be demonstrated, in addition to addressing temporal resolution of lifetime-based approaches.
- The primary drawback of Ln-NPs associated with the relatively poor emission intensities of these materials stems from the low absorption cross-section and the forbidden nature of the Ln^{3+} 4f–4f electronic transitions. A promising strategy to overcome this drawback might be the combination of Ln-NPs with sensitizers, such as semiconductor QDs.[125,126]
- Seeking self-calibrating nanothermometers, while some promising examples exist,[127,128] future directions may include a more in-depth exploration of hybrid materials that combine Ln-NPs with non-Ln materials fully operating in the NIR spectral region. By using the emission generated by the non-Ln material as a calibration band for the temperature-dependent emission of the Ln-NP, a so called 'self-referencing' nanothermometer can be developed and limitations often encountered regarding recalibration can be minimized.
- Last but not least, while emerging, NIR-NIR nanothermometry is still behind developments made with respect to nanothermometry based on NIR-to-visible upconversion, including fundamental studies that unveil challenges such as the interplay between photonic effects and thermal performance.[129] Thus, ideally, lessons learned from those investigations would also be considered for the development of next-generation NIR-NIR nanothermometers.

Despite remaining challenges, in light of the tremendous advancement of the field from its first steps a little more than two decades ago to major achievements made during the most recent years, one may be confident that existing gaps in fundamental understanding can be closed to bring Ln^{3+}-based thermal sensors to real-life application. For this to be achieved further efforts will have to be undertaken to address the now well-identified challenges (and those unknown ones that will most certainly arise in the future). If researchers in chemistry, physics, and materials science collaborate effectively, significant progress can be achieved, addressing the hurdles that lie ahead. Overcoming barriers between the natural sciences and medicine and extending collaboration with clinicians will be required to integrate nanothermometry into clinical trials and discoveries into real-life applications. In addition, engaging experts in artificial intelligence and machine learning may be expected to play a pivotal role in the design of next-generation NIR-NIR nanothermometers.

Author contributions

All authors have contributed to original draft writing and revision of the manuscript.

Conflicts of interest

There are no conflicts to declare.

Acknowledgements

A. P. is thankful for the financial support provided by the National Research Council Canada (NRC, QSP 045-1). N. L. is thankful for financial support provided by China Scholarship Council (CSC).

References

1 J. Zhou, B. Del Rosal, D. Jaque, S. Uchiyama and D. Jin, *Nat. Methods*, 2020, **17**, 967–980.
2 C. D. S. Brites, S. Balabhadra and L. D. Carlos, *Adv. Opt. Mater.*, 2018, **7**, 1801239.
3 C. Bradac, S. F. Lim, H. C. Chang and I. Aharonovich, *Adv. Opt. Mater.*, 2020, **8**, 202000183.
4 B. del Rosal, E. Ximendes, U. Rocha and D. Jaque, *Adv. Opt. Mater.*, 2017, **5**, 1600508.
5 C. D. S. Brites, A. Millán and L. D. Carlos, Lanthanides in Luminescent Thermometry, in *Handbook on the Physics and Chemistry of Rare Earths*, ed. J. C. G. Bunzli and V. K. Pecharsky, Elsevier Science, B. V., Amsterdam, 2016, pp. 339.
6 D. Jaque and F. Vetrone, *Nanoscale*, 2012, **4**, 4301–4326.
7 C. D. Brites, P. P. Lima, N. J. Silva, A. Millan, V. S. Amaral, F. Palacio and L. D. Carlos, *Nanoscale*, 2012, **4**, 4799–4829.
8 C. D. S. Brites, R. Marin, M. Suta, A. N. C. Neto, E. Ximendes, D. Jaque and L. D. Carlos, *Adv. Mater.*, 2023, **35**, 2302749.
9 X. D. Wang, O. S. Wolfbeis and R. J. Meier, *Chem. Soc. Rev.*, 2013, **42**, 7834–7869.
10 S. W. Allison, *Meas. Sci. Technol.*, 2019, **30**, 072001.
11 M. Quintanilla, M. Henriksen-Lacey, C. Renero-Lecuna and L. M. Liz-Marzan, *Chem. Soc. Rev.*, 2022, **51**, 4223–4242.
12 D. A. Gálico, C. M. S. Calado and M. Murugesu, *Chem. Sci.*, 2023, **14**, 5827–5841.
13 Y. Hasegawa and Y. Kitagawa, *J. Mater. Chem. C*, 2019, **7**, 7494–7511.

14 L. Aldaz-Caballero, U. R. Rodríguez-Mendoza, V. Lavín, P. Canton, A. Benayas and R. Marin, *Adv. Sens. Res.*, 2023, **2**, 202300078.

15 R. Marin, N. C. Millan, L. Kelly, N. Liu, E. M. Rodrigues, M. Murugesu and E. Hemmer, *J. Mater. Chem. C*, 2022, **10**, 1767–1775.

16 W. U. Khan, L. Qin, A. Alam, P. Zhou, Y. Peng and Y. Wang, *ACS Appl. Bio Mater.*, 2021, **4**, 5786–5796.

17 A. A. Ansari, A. K. Parchur, M. K. Nazeeruddin and M. M. Tavakoli, *Coord. Chem. Rev.*, 2021, **444**, 214040.

18 M. Jia, X. Chen, R. Sun, D. Wu, X. Li, Z. Shi, G. Chen and C. Shan, *Nano Res.*, 2022, **16**, 2949–2967.

19 J. C. Bunzli and C. Piguet, *Chem. Soc. Rev.*, 2005, **34**, 1048–1077.

20 L. Labrador-Paez, M. Pedroni, A. Speghini, J. Garcia-Sole, P. Haro-Gonzalez and D. Jaque, *Nanoscale*, 2018, **10**, 22319–22328.

21 J. F. Algorri, M. Ochoa, P. Roldan-Varona, L. Rodriguez-Cobo and J. M. Lopez-Higuera, *Cancers*, 2021, **13**, 4447.

22 A. Skripka, A. Morinvil, M. Matulionyte, T. Cheng and F. Vetrone, *Nanoscale*, 2019, **11**, 11322–11330.

23 A. Nexha, J. J. Carvajal, M. C. Pujol, F. Díaz and M. Aguiló, *J. Mater. Chem. C*, 2020, **8**, 180–191.

24 M. A. Hernandez-Rodriguez, A. D. Lozano-Gorrin, V. Lavin, U. R. Rodriguez-Mendoza and I. R. Martin, *Opt. Express*, 2017, **25**, 27845–27856.

25 A. F. Pereira, J. F. Silva, A. S. Gouveia-Neto and C. Jacinto, *Sens. Actuators, B*, 2017, **238**, 525–531.

26 C. Hazra, A. Skripka, S. J. L. Ribeiro and F. Vetrone, *Adv. Opt. Mater.*, 2020, **8**, 2001178.

27 A. Ćirić, T. van Swieten, J. Periša, A. Meijerink and M. D. Dramićanin, *J. Appl. Phys.*, 2023, **133**, 194501.

28 A. Puccini, N. Liu and E. Hemmer, *ACS Mater. Lett.*, 2024, **6**, 1327–1337.

29 B. Zhang, X. Guo, Z. Zhang, Z. Fu and H. Zheng, *J. Lumin.*, 2022, **250**, 119089.

30 S. Golovynskyi, I. Golovynska, L. I. Stepanova, O. I. Datsenko, L. Liu, J. Qu and T. Y. Ohulchanskyy, *J. Biophotonics*, 2018, **11**, 201800141.

31 L. A. Sordillo, Y. Pu, S. Pratavieira, Y. Budansky and R. R. Alfano, *J. Biomed. Opt.*, 2014, **19**, 056004.

32 E. Hemmer, A. Benayas, F. Legare and F. Vetrone, *Nanoscale Horiz.*, 2016, **1**, 168–184.

33 Z. Feng, T. Tang, T. Wu, X. Yu, Y. Zhang, M. Wang, J. Zheng, Y. Ying, S. Chen, J. Zhou, X. Fan, D. Zhang, S. Li, M. Zhang and J. Qian, *Light: Sci. Appl.*, 2021, **10**, 197.

34 J. A. Carr, M. Aellen, D. Franke, P. T. C. So, O. T. Bruns and M. G. Bawendi, *Proc. Natl. Acad. Sci. U. S. A.*, 2018, **115**, 9080–9085.

35 M. Tanzid, N. J. Hogan, A. Sobhani, H. Robatjazi, A. K. Pediredla, A. Samaniego, A. Veeraraghavan and N. J. Halas, *ACS Photonics*, 2016, **3**, 1787–1793.

36 L. H. Fischer, G. S. Harms and O. S. Wolfbeis, *Angew. Chem., Int. Ed.*, 2011, **50**, 4546–4551.

37 A. Bednarkiewicz, L. Marciniak, L. D. Carlos and D. Jaque, *Nanoscale*, 2020, **12**, 14405–14421.

38 A. Nexha, J. J. Carvajal, M. C. Pujol, F. Diaz and M. Aguilo, *Nanoscale*, 2021, **13**, 7913–7987.

39 H. Suo, X. Zhao, Z. Zhang, Y. Wang, J. Sun, M. Jin and C. Guo, *Laser Photonics Rev.*, 2020, **15**, 2000319.

40 F. Vetrone, R. Naccache, A. Zamarro, A. J. de la Fuente, F. Sanz-Rodrıguez, L. M. Maestro, E. M. Rodriguez, D. Jaque, J. G. Sole and J. A. Capobianco, *ACS Nano*, 2010, **4**, 3254–3258.

41 T. P. van Swieten, A. Meijerink and F. T. Rabouw, *ACS Photonics*, 2022, **9**, 1366–1374.

42 M. Suta, Z. Antic, V. Ethordevic, S. Kuzman, M. D. Dramicanin and A. Meijerink, *Nanomaterials*, 2020, **10**, 10030543.

43 A. S. Laia, D. A. Hora, M. V. d. S. Rezende, M. A. Gomes, A. C. Brandão-Silva, M. A. C. d. Santos, N. O. Dantas, A. C. A. Silva, J. J. Rodrigues, M. E. G. Valerio, Z. S. Macedo and M. A. R. C. Alencar, *Photonics*, 2023, **10**, 485.

44 Y. Shen, J. Lifante, N. Fernandez, D. Jaque and E. Ximendes, *ACS Nano*, 2020, **14**, 4122–4133.

45 M. Runowski, P. Wozny, N. Stopikowska, I. R. Martin, V. Lavin and S. Lis, *ACS Appl. Mater. Interfaces*, 2020, **12**, 43933–43941.

46 J. Perisa, Z. Ristic, W. Piotrowski, Z. Antic, L. Marciniak and M. D. Dramicanin, *RSC Adv.*, 2021, **11**, 15933–15942.

47 M. E. Raab, S. L. Maurizio, J. A. Capobianco and P. N. Prasad, *J. Phys. Chem. B*, 2021, **125**, 13132–13136.

48 M. Kong, Y. Gu, Y. Chai, J. Ke, Y. Liu, X. Xu, Z. Li, W. Feng and F. Li, *Sci. China: Chem.*, 2021, **64**, 974–984.

49 M. Tan, F. Li, N. Cao, H. Li, X. Wang, C. Zhang, D. Jaque and G. Chen, *Small*, 2020, **16**, 2004118.

50 Y. Sun, M. Kong, J. Ke, W. Yuan, C. Wen, Y. Gu, S. Luo and W. Feng, *ACS Appl. Nano Mater.*, 2023, **6**, 23173–23183.

51 M. Matulionyte, A. Skripka, A. Ramos-Guerra, A. Benayas and F. Vetrone, *Chem. Rev.*, 2023, **123**, 515–554.

52 X. Xie, N. Gao, R. Deng, Q. Sun, Q. H. Xu and X. Liu, *J. Am. Chem. Soc.*, 2013, **135**, 12608–12611.

53 Y. F. Wang, G. Y. Lin, L. D. Sun, J. W. Xiao, J. C. Zhou and C. H. Yan, *ACS Nano*, 2013, **7**, 7200–7206.

54 J. Shen, G. Chen, A.-M. Vu, W. Fan, O. S. Bilsel, C.-C. Chang and G. Han, *Adv. Opt. Mater.*, 2013, **1**, 644–650.

55 C. Renero-Lecuna, A. Herrero, D. J. de Aberasturi, M. Martinez-Florez, R. Valiente, M. Mychinko, S. Bals and L. M. Liz-Marzan, *J. Phys. Chem. C*, 2021, **125**, 19887–19896.

56 K. Hamraoui, V. A. Torres-Vera, I. Zabala Gutierrez, A. Casillas-Rubio, M. Alqudwa Fattouh, A. Benayas, R. Marin, M. M. Natile, M. Manso Silvan, J. Rubio-Zuazo, D. Jaque, S. Melle, O. G. Calderon and J. Rubio-Retama, *ACS Appl. Mater. Interfaces*, 2023, **15**, 32667–32677.

57 N. Rakov and G. S. Maciel, *J. Appl. Phys.*, 2017, **121**, 113103.

58 P. M. Gschwend, F. H. L. Starsich, R. C. Keitel and S. E. Pratsinis, *Chem. Commun.*, 2019, **55**, 7147–7150.

59 X. Yuan, E. Cui, K. Liu, Y. Jiang, X. Yang, J. Tang, L. Yang, X. Liao, Y. Zhao, W. Sun, Y. Liu and J. Liu, *Ceram. Int.*, 2022, **48**, 35141–35149.

60 T. Grzyb, I. R. Martin and R. Popescu, *Nanoscale*, 2024, **16**, 1692–1702.

61 L. Marciniak, K. Waszniewska, A. Bednarkiewicz, D. Hreniak and W. Strek, *J. Phys. Chem. C*, 2016, **120**, 8877–8882.

62 D. Kobat, N. Nishimura, A. W. Wong, C. B. Schaffer and C. Xu, *Opt. Express*, 2009, **17**, 13354–13364.

63 I. V. Barbosa, L. J. Q. Maia, A. Ibanez and G. Dantelle, *Opt. Mater.: X*, 2023, **18**, 100236.

64 L. Labrador-Páez, U. Kostiv, J. Widengren and H. Liu, *Adv. Opt. Mater.*, 2022, **13**, 11208–11215.

65 S. L. Jacques, *Phys. Med. Biol.*, 2013, **58**, 5007–5008.

66 B. del Rosal, A. Pérez-Delgado, M. Misiak, A. Bednarkiewicz, A. S. Vanetsev, Y. Orlovskii, D. J. Jovanović, M. D. Dramićanin, U. Rocha, K. Upendra Kumar, C. Jacinto, E. Navarro, E. M. Rodríguez, M. Pedroni, A. Speghini, G. A. Hirata, I. R. Martín and D. Jaque, *J. Appl. Phys.*, 2015, **118**, 14304.

67 I. Villa, A. Vedda, I. X. Cantarelli, M. Pedroni, F. Piccinelli, M. Bettinelli, A. Speghini, M. Quintanilla, F. Vetrone, U. Rocha, C. Jacinto, E. Carrasco, F. S. Rodríguez, Á. Juarranz, B. del Rosal, D. H. Ortgies, P. H. Gonzalez, J. G. Solé and D. J. García, *Nano Res.*, 2014, **8**, 649–665.

68 E. Ximendes, R. Marin, L. D. Carlos and D. Jaque, *Light: Sci. Appl.*, 2022, **11**, 237.

69 B. Del Rosal, I. Villa, D. Jaque and F. Sanz-Rodriguez, *J. Biophotonics*, 2016, **9**, 1059–1067.

70 A. M. Smith, M. C. Mancini and S. Nie, *Nat. Nanotechnol.*, 2009, **4**, 710–711.

71 X. Luo, C. Zhang, Z. Yu, S. Wen and Y. Xian, *TrAC, Trends Anal. Chem.*, 2023, **169**, 117368.

72 A. Skripka, A. Benayas, R. Marin, P. Canton, E. Hemmer and F. Vetrone, *Nanoscale*, 2017, **9**, 3079–3085.

73 Y. Wang, L. Lei, E. Liu, Z. Lu and S. Xu, *Opt. Commun.*, 2022, **510**, 127935.

74 M. Jia, Z. Fu, G. Liu, Z. Sun, P. Li, A. Zhang, F. Lin, B. Hou and G. Chen, *Adv. Opt. Mater.*, 2020, **8**, 1901173.

75 K. Maciejewska, A. Bednarkiewicz and L. Marciniak, *Phys. B*, 2021, **620**, 413247.

76 H. Xu, M. Jia, Z. Wang, Y. Wei and Z. Fu, *ACS Appl. Mater. Interfaces*, 2021, **13**, 61506–61517.

77 Y. Lu, Y. Li, J. Li, D. Lin, H. Lu and H. Zou, *J. Lumin.*, 2023, **263**, 120067.

78 Y. Sun, W. Feng, P. Yang, C. Huang and F. Li, *Chem. Soc. Rev.*, 2015, **44**, 1509–1525.

79 L. Marciniak, A. Bednarkiewicz, M. Stefanski, R. Tomala, D. Hreniak and W. Strek, *Phys. Chem. Chem. Phys.*, 2015, **17**, 24315–24321.

80 Q. Hu, N. Kong, Y. Chai, Z. Xing, Y. Wu, J. Zhang, F. Li and X. Zhu, *Nanoscale Horiz.*, 2022, **7**, 1177–1185.

81 L. Wortmann, S. Suyari, T. Ube, M. Kamimura and K. Soga, *J. Lumin.*, 2018, **198**, 236–242.

82 S. Balabhadra, M. L. Debasu, C. D. S. Brites, R. A. S. Ferreira and L. D. Carlos, *J. Phys. Chem. C*, 2017, **121**, 13962–13968.

83 L. Labrador-Paez, E. C. Ximendes, P. Rodriguez-Sevilla, D. H. Ortgies, U. Rocha, C. Jacinto, E. M. Rodriguez, P. Haro-Gonzalez and D. Jaque, *Nanoscale*, 2018, **10**, 12935–12956.

84 S. Liu, J. Ueda and S. Tanabe, *Appl. Phys. Lett.*, 2023, **123**, 161101.

85 A. Ćirić, S. Stojadinović and M. D. Dramićanin, *Sens. Actuators, A*, 2019, **295**, 450–455.

86 L. Wu and G. Chen, Luminescence Lifetime Nanothermometry for Accurate Temperature Measurements In Vivo, in *Luminescent Thermometry*, ed. J. J. Carvajal Martí and M. C. Pujol Baiges, Springer, 2023, pp. 283–298.

87 D. H. Ortgies, M. Tan, E. C. Ximendes, B. Del Rosal, J. Hu, L. Xu, X. Wang, E. M. Rodriguez, C. Jacinto, N. Fernandez, G. Chen and D. Jaque, *ACS Nano*, 2018, **12**, 4362–4368.

88 K. T. V. Grattan and A. W. Palmer, *Rev. Sci. Instrum.*, 1985, **56**, 1784–1787.

89 H. W. S. Hong Shang Peng, Bao Jiu Chen, Ji Wei Wang, Shao Zhe Lu, Xiang Gui Kong and a. J. H. Zhang, *J. Chem. Phys.*, 2002, **18**, 6.

90 X. M. Guo, H. H. Song, E. Zhang, C. Combs, N. Clemens, X. S. Chen, K. K. Li, Y. Zou and H. Jiang, *Sens. Transducers J.*, 2011, **13**, 124–130.

91 K. Maciejewska, A. Bednarkiewicz and L. Marciniak, *Nanoscale Adv.*, 2021, **3**, 4918–4925.

92 K. Maciejewska, M. Szalkowski, A. Bednarkiewicz and L. Marciniak, *J. Mater. Chem. C*, 2021, **9**, 15831–15839.

93 L. Wu, M. Jia, D. Li and G. Chen, *Nano Lett.*, 2023, **23**, 2862–2869.

94 X. Qiu, Q. Zhou, X. Zhu, Z. Wu, W. Feng and F. Li, *Nat. Commun.*, 2020, **11**, 1–9.

95 S. Balabhadra, P. S. Solanki, M. F. Reid and J.-P. R. Wells, *Opt. Laser Technol.*, 2024, **171**, 110438.

96 D. Avram, I. Porosnicu, A. Patrascu and C. Tiseanu, *Adv. Photonics Res.*, 2022, **3**, 2100208.

97 Q. Wang, M. Liao, Q. Lin, M. Xiong, Z. Mu and F. Wu, *J. Alloys Compd.*, 2021, **850**, 156744.

98 L. Marciniak, A. Bednarkiewicz, K. Trejgis, K. Maciejewska, K. Elzbieciak and K. Ledwa, *Phys. Chem. Chem. Phys.*, 2019, **21**, 10532–10539.

99 A. Paściak, M. Misiak, K. Trejgis, K. Elżbieciak-Piecka, O. Bezkrovnyi, Ł. Marciniak and A. Bednarkiewicz, *J. Alloys Compd.*, 2023, **934**, 167900.

100 E. Hemmer, P. Acosta-Mora, J. Mendez-Ramos and S. Fischer, *J. Mater. Chem. B*, 2017, **5**, 4365–4392.

101 L. Marciniak, W. M. Piotrowski, M. Szymczak, M. Pieprz and K. Trejgis, New Strategies to Improve Thermal Sensitivity and Temperature Resolution in Lanthanide-Doped Luminescent Thermometers, in *Luminescent*

Thermometry, ed. J. J. Carvajal Martí and M. C. Pujol Baiges, Springer, 2023, pp. 69–103.

102 O. A. Savchuk, J. J. Carvajal, P. Haro-Gonzalez, M. Aguiló and F. Díaz, *J. Alloys Compd.*, 2018, **746**, 710–719.

103 O. A. Savchuk, J. J. Carvajal, M. C. Pujol, J. Massons, P. Haro-González, O. Martínez, J. Jiménez, M. Aguiló and F. Díaz, *J. Lumin.*, 2016, **169**, 711–716.

104 O. A. Savchuk, P. Haro-Gonzalez, J. J. Carvajal, D. Jaque, J. Massons, M. Aguilo and F. Diaz, *Nanoscale*, 2014, **6**, 9727–9733.

105 H. Suo, C. Guo, J. Zheng, B. Zhou, C. Ma, X. Zhao, T. Li, P. Guo and E. M. Goldys, *ACS Appl. Mater. Interfaces*, 2016, **8**, 30312–30319.

106 H. Suo, X. Zhao, Z. Zhang, R. Shi, Y. Wu, J. Xiang and C. Guo, *Nanoscale*, 2018, **10**, 9245–9251.

107 W. Xu, S. Zong, F. Shang, L. Zheng and Z. Zhang, *Photonics Res.*, 2022, **10**, 2532–2540.

108 A. C. C. Soares, T. O. Sales, E. C. Ximendes, D. Jaque and C. Jacinto, *Nanoscale Adv.*, 2023, **5**, 3664–3670.

109 J. Zhou, B. Huang, Z. Yan and J. G. Bunzli, *Light: Sci. Appl.*, 2019, **8**, 84.

110 D. G. Stone, Y. Chen, E. A. Ekimov, T. T. Tran and C. Bradac, *ACS Appl. Opt. Mater.*, 2023, **1**, 898–905.

111 Z. Liang, J. Wu, Y. Cui, H. Sun and C. Z. Ning, *Light: Sci. Appl.*, 2023, **12**, 36.

112 E. P. Santos, R. S. Pugina, E. G. Hilário, A. J. A. Carvalho, C. Jacinto, F. A. M. G. Rego-Filho, A. Canabarro, A. S. L. Gomes, J. M. A. Caiut and A. L. Moura, *Sens. Actuators, A*, 2023, **362**, 114666.

113 M. Tan, F. Li, X. Wang, R. Fan and G. Chen, *ACS Nano*, 2020, **14**, 6532–6538.

114 A. Nexha, M. C. Pujol Baiges and J. J. Carvajal Martí, Luminescent Nanothermometers Operating Within Biological Windows, in *Luminescent Thermometry*, ed. J. J. Carvajal Martí and M. C. Pujol Baiges, Springer, 2023, pp. 221–268.

115 T. Bai and N. Gu, *Small*, 2016, **12**, 4590–4610.

116 B. Gidwani, V. Sahu, S. S. Shukla, R. Pandey, V. Joshi, V. K. Jain and A. Vyas, *J. Drug Delivery Sci. Technol.*, 2021, **61**, 102308.

117 Y. Liang, T. Zhang and M. Tang, *J. Appl. Toxicol.*, 2022, **42**, 17–40.

118 R. Marin, A. Vivian, A. Skripka, A. Migliori, V. Morandi, F. Enrichi, F. Vetrone, P. Ceroni, C. Aprile and P. Canton, *ACS Appl. Nano Mater.*, 2019, **2**, 2426–2436.

119 H. Zhang, Y. Wu, Z. Gan, Y. Yang, Y. Liu, P. Tang and D. Wu, *J. Mater. Chem. B*, 2019, **7**, 2835–2844.

120 M. P. Ogáyar, D. Mendez-Gonzalez, I. Z. Gutierrez, A. Artiga, J. Rubio-Retama, O. G. Calderon, S. Melle, A. Serrano, A. Espinosa, D. Jaque and R. Marin, *Nanoscale*, 2023, **15**, 17956–17962.

121 L. Marciniak, K. Kniec, K. Elżbieciak-Piecka, K. Trejgis, J. Stefanska and M. Dramićanin, *Coord. Chem. Rev.*, 2022, **469**, 214671.

122 W. M. Piotrowski, R. Marin, M. Szymczak, E. M. Rodríguez, D. H. Ortgies, P. Rodríguez-Sevilla, M. D. Dramićanin, D. Jaque and L. Marciniak, *Adv. Opt. Mater.*, 2022, **11**, 2202366.

123 M. Raab, A. Skripka, J. Bulmahn, A. Pliss, A. Kuzmin, F. Vetrone and P. Prasad, *ACS Appl. Bio Mater.*, 2022, **5**, 4948–4954.

124 N. Liu, C. Homann, S. Morfin, M. S. Kesanakurti, N. D. Calvert, A. J. Shuhendler, T. Al and E. Hemmer, *Nanoscale*, 2023, **15**, 19546–19556.

125 R. Marin, D. Jaque and A. Benayas, *Nanoscale Horiz.*, 2021, **6**, 209–230.

126 R. Marin and D. Jaque, *Chem. Rev.*, 2021, **121**, 1425–1462.

127 C. D. S. Brites, E. D. Martinez, R. R. Urbano, C. Rettori and L. D. Carlos, *Front. Chem.*, 2019, **7**, 267.

128 A. M. P. Botas, C. D. S. Brites, J. Wu, U. Kortshagen, R. N. Pereira, L. D. Carlos and R. A. S. Ferreira, *Part. Part. Syst. Charact.*, 2016, **33**, 740–748.

129 S. J. W. Vonk, T. P. van Swieten, A. Cocina and F. T. Rabouw, *Nano Lett.*, 2023, **23**, 6560–6566.